Astronomy & Astrophysics manuscript no. optf˙astroph February 25, 2005
(DOI: will be inserted by hand later)

The Chandra Deep Field South/GOODS survey ⋆

Optically faint X-ray sources

V. Mainieri[1,2,3], P. Rosati[2], P. Tozzi[4], J. Bergeron[5], R. Gilli[6], G. Hasinger[1], M. Nonino[4], I. Lehmann[1], D.M. Alexander[7], R. Idzi[8], A.M. Koekemoer[8], C. Norman[9], G. Szokoly[1], and W. Zheng[9]

[1] Max-Planck-Institut für extraterrestrische Physik, Giessenbachstrasse PF 1312, 85748 Garching bei Muenchen, Germany
[2] European Southern Observatory, Karl-Schwarzschild-Strasse 2, D-85748 Garching, Germany
[3] Dip. di Fisica, Università degli Studi Roma Tre, Via della Vasca Navale 84, I-00146 Roma, Italy
[4] INAF, Osservatorio Astronomico di Trieste, via G.B. Tiepolo 11, I-34131, Trieste, Italy
[5] Institut d'Astrophysique de Paris, 98bis Boulevard, F-75014 Paris, France
[6] INAF, Osservatorio Astrofisico di Arcetri, Largo E. Fermi 5, I-50125, Firenze, Italy
[7] Institute of Astronomy, Madingley Road, Cambridge CB3 0HA, UK
[8] Space Telescope Science Institute, 3700 San Martin Drive, Baltimore, MD 21218, USA
[9] Center for Astrophysical Sciences, Department of Physics and Astronomy, The Johns Hopkins University, Baltimore, MD 21218, USA

Received 2 May 2004; Accepted 25 May 2005

Abstract. We provide important new constraints on the nature and redshift distribution of optically faint (R$\geq$ 25) X-ray sources in the Chandra Deep Field South Survey. We use a large multi-wavelength data set, including the GOODS/ACS survey, the recently released Hubble Ultra Deep Field (UDF) data, and the new public VLT/ISAAC imaging. We show that we can derive accurate photometric redshifts for the spectroscopically unidentified sources thus maximizing the redshift completeness for the whole X-ray sample. Our new redshift distribution for the X-ray source population is in better agreement with that predicted by X-ray background synthesis models; however, we still find an overdensity of low redshift (z$<$ 1) sources. The optically faint sources are mainly X-ray absorbed AGN, as determined from direct X-ray spectral analysis and other diagnostics.
Many of these optically faint sources have high ($>$ 10) X-ray-to-optical flux ratios. We also find that $\sim$ 71% of them are well fitted with the SED of an early-type galaxy with $<z_{\rm phot}>\sim$ 1.9 and the remaining 29% with irregular or starburst galaxies mainly at $z_{\rm phot} > 3$. We estimate that 23% of the optically faint sources are X-ray absorbed QSOs. The overall population of X-ray absorbed QSOs contributes a $\sim$ 15% fraction of the [2-10] keV X-ray Background (XRB) whereas current XRB synthesis models predict a $\sim$ 38% contribution.

Key words. Surveys – Galaxies: active – *(Galaxies:)* quasars: general – *(Cosmology:)* diffuse radiation – X-ray: galaxies – X-rays: general

1. Introduction

Recent *Chandra* and XMM-*Newton* (Brandt et al. 2001, Rosati et al. 2002, Hasinger et al. 2001) deep surveys have almost resolved the entire $2-10$ keV X-ray background (XRB), forty years after its discovery (Giacconi et al. 1962). A large optical follow-up program of hundreds of X-ray sources in these fields has lead to the identification of a mixture of obscured and unobscured AGN, with an increasing fraction of obscured AGN at faint X-ray fluxes (Barger et al. 2003, Szokoly et al. 2004). The optical counterparts of a significant fraction of the X-ray sources are too faint (R$\geq$25) for optical spectroscopy, even for $\approx 5-6$ hours exposures with 8-10 m class telescopes. In this work, we focus on this subsample of X-ray sources with R$\geq$ 25, which will be referred to as *Optically Faint Sources* (OFS). This criterium

Send offprint requests to: V. Mainieri, e-mail: vmainieri@mpe.mpg.de

⋆ Based in part on observations obtained at the European Southern Observatory using the ESO Very Large Telescope on Cerro Paranal (ESO program 168.A-0485)

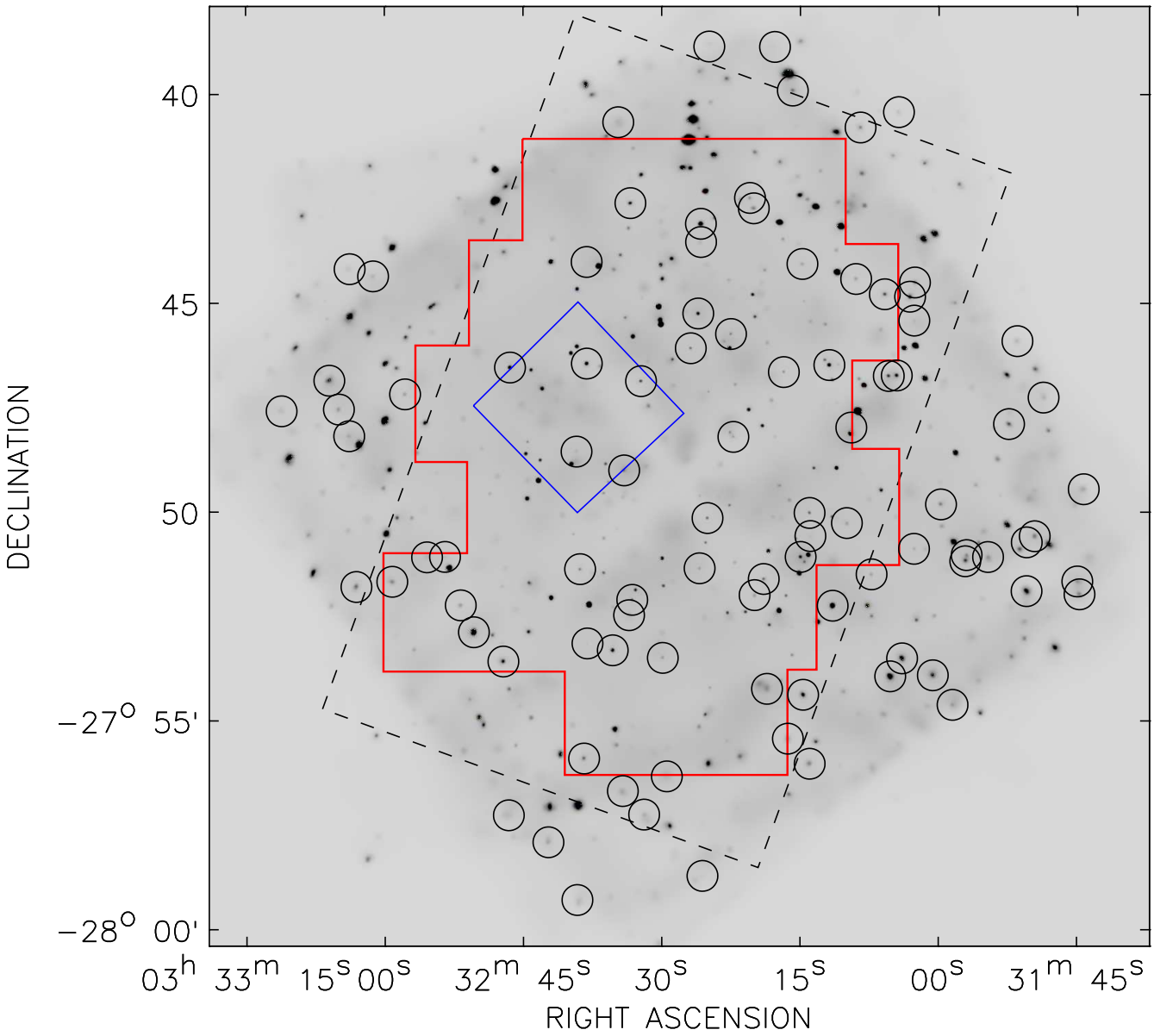

Fig. 1. Adaptively smoothed Chandra image of the CDF-S in the [0.5-7] keV band. The circles show the position of OFS. The big dashed rectangle is the area of the GOODS survey (*"GOODS area"*); the polygon indicates the region of the deep public VLT/ISAAC observations currently available and the small square indicates the area of the Hubble Ultra Deep Field (UDF).

simply reflects an observational limit beyond which we need to rely on accurate photometric measurements and X-ray spectral information to estimate their redshift and to establish their physical nature. We note that OFS represent a quarter of the entire X-ray sample, therefore they have a significant impact on statistical studies, such as the X-ray luminosity function, the evolution of the TypeI/TypeII ratio and the overall N_H distribution. Moreover, many OFS are relatively bright in the X-ray band, due to powerful AGN activity [Alexander et al. (2001); Mignoli et al. (2004)]. It is possible that a sizeble fraction of these sources belong to the long-sought class of high-redshift, high luminosity, heavily obscured active galactic nuclei (Type II QSOs).

The first detailed study of OFS has been done by Alexander et al. (2001) in the Chandra Deep Field Nord (CDF-N). Here we extend that work by estimating photometric redshifts for a large fraction of the OFS population, providing

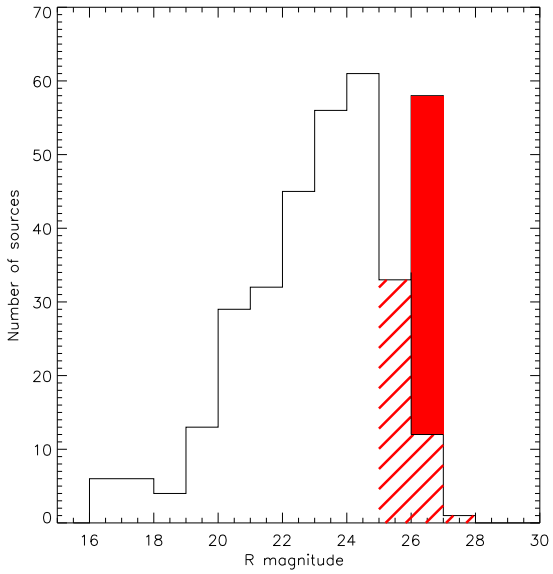

Fig. 2. The R-band magnitude distribution for the optical counterparts of the X-ray sample. The hatched box are the OFS, while the shaded part refers to the sources without a R band counterparts (down to R= 26.7).

direct constraints on their intrinsic absorption and on their spectral energy distribution.
The outline of the paper is as follows: in §2 we describe the X-ray sample. In §3 we compare the X-ray properties of the optically bright (R<25) and faint (R≥25) X-ray sources. In §4 we derive photometric redshifts. In §5 we discuss the few OFS with known spectroscopic redshifts. In §6 we use the X-ray to optical flux ratios as a diagnostic tool. In §7 we perform an X-ray spectral analysis and in §8 we derive the fraction of OFS that are likely to be X-ray detected Type-2 QSOs. We study in detail the OFS inside the Hubble Ultra Deep Field in §9. Finally in §10 we summarize and discuss the results. Throughout this paper we use Vega magnitudes (if not otherwise stated) and assume $\Omega_{\rm M} = 0.3$, $\Omega_{\Lambda} = 0.7$ and $\rm H_0 = 70$ km/s/Mpc.

2. The sample

The X-ray sample is obtained from the 1 Ms *Chandra* observation of the Chandra Deep Field South (CDF-S; Giacconi et al. 2002; Rosati et al. 2002). We refer to Table 2 in Giacconi et al. (2002) for the X-ray quantities and relative errors (e.g., X-ray fluxes, counts). In Figure 1 we show a smoothed 0.5-7 keV image of the CDF-S field on which we have highlighted the OFS. The distribution of R band magnitudes for the X-ray sources is reported in Figure 2. From the entire X-ray sample of 346 sources, 92 are OFS ($\sim$ 27%), of which 46 ($\sim$ 13% of the total sample) do not have a R band counterpart (down to R=26.1-26.7). In the CDF-N, the fraction of optically faint sources (I$\geq$ 24) is slightly larger ($\approx$ 33%; Alexander et al. 2001); however, this study was performed in the most sensitive region of the CDF-N field, while here we are considering the whole of the CDF-S field.
At present only six ($\sim$ 6%) of the OFS have been spectroscopically identified, as compared to 151 ($\sim$ 60%) of the optically bright (R$<$ 25) X-ray sources (Szokoly et al. 2004). We will discuss in detail the properties of these six OFS in Section 5. For the remaining OFS it will be challenging to obtain a spectroscopic redshift with 8-10 meter telescopes, with the exception of those sources with strong emission lines. In order to obtain information on their redshift distribution we have determined photometric redshifts (see Section 4).

3. Comparison of the optically bright and optically faint X-ray source samples

Before we investigate in detail the nature of the optically faint X-ray source population, we will compare their general X-ray properties with those of the well-studied optically bright X-ray source population (see also Section 4 of Alexander et al. 2001).

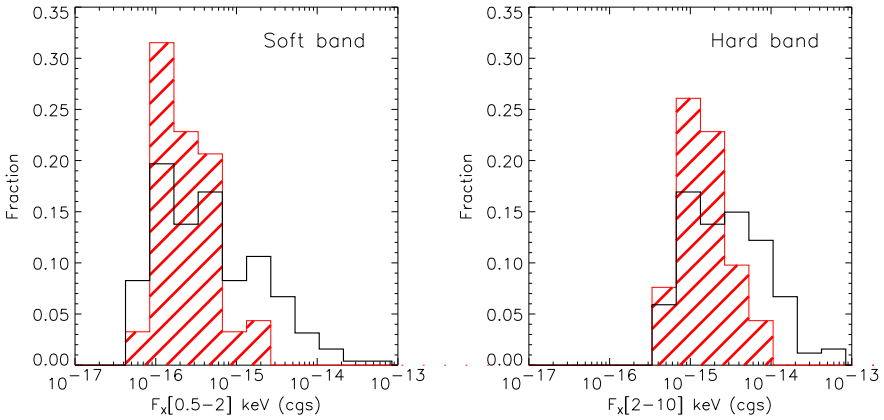

Fig. 3. The distributions of X-ray fluxes in the 0.5-2 keV (left panel) and 2-10 keV band (right panel) for the OFS (hatched histogram) and optically bright sources (open histogram).

3.1. X-ray fluxes

In Figure 3 we compare the X-ray fluxes distributions of the optically bright and faint sources in the 0.5−2 keV (left panel) and 2−10 keV bands (right panel). According to a Kolmogorov-Smirnov test the probability that the distributions are drawn from the same population is extremely small ($\sim 0.02\%$ in the 0.5-2 keV band and $\sim 0.001\%$ in the 2-10 keV band). According to Figure 3, almost all the bright X-ray sources are part of the optically bright sample.

The total flux in the 2-10 keV band of the OFS is $\sim 1.6 \times 10^{-12}$ erg cm^{-2} s^{-1} deg^{-2} after correcting for the sky coverage in the CDF-S (see Fig. 5 of Giacconi et al. 2002). This accounts for a $\sim 7-10\%$ fraction of the [2-10] keV XRB; the estimated error range corresponds to the uncertainty in the measurement of the XRB flux (HEAO−1, Marshall et al. 1980 and Revnivtsev et al. 2004; SAX, Vecchi et al. 1999; XMM-*Newton*, De Luca & Molendi 2004).

3.2. Hardness ratios distibution

The hardness ratio (HR) is a useful tool to characterize the spectral shape of the AGN X-ray continuum. We adopt the definition HR≡(H−S)/(H+S), where H and S are the net count rates in the 2-7 keV and 0.5-2 keV band, respectively. We have recomputed the HR values over those given in Giacconi et al. (2002) by performing aperture photometry for each source in both the 0.5-2 keV and 2-10 keV bands irregardless of whether the source is detected in either of these bands. Therefore, several values previously set to +1 or −1 (Giacconi et al. 2002) have a different value, still consistent with the old one within 1σ error. When HR= ± 1, we plot the 1σ upper/lower limits. Other minor differences come from the new reduction of the CDF-S data performed after the release of CALDB 2.26 and CIAO3.1. In particular, we applied the correction for the degraded effective area of ACIS–I chips due to material accumulated on the ACIS optical blocking filter at the epoch of the observation using the recently released time–dependent gain correction (see http://asc.harvard.edu/ciao/threads/acistimegain/).
We have corrected the HR values for the off-axis angle of the source, normalizing the soft and hard counts to refer to an on-axis source falling on the aimpoint (chip3). To do that, we have used the soft and hard exposure maps computed for the monochromatic energies of 1.5 and 4.5 keV respectively.

In Figure 4 we show the hardness ratio distributions. A larger fraction of OFS show a high HR, typical of intrinsically absorbed AGN emission, than found in the optically bright sample.[1] The two HR distributions are distinguishable according to the Kolmogorov-Smirnov test at the 98% significance level; a similar result has been obtained by Alexander et al. (2001) in the CDF-N. These findings are also in agreement with the general trend toward flatter X-ray spectral slopes at fainter X-ray fluxes (i.e. Tozzi et al. 2001). It has been shown that this flattening is due to the fainter X-ray sources having more absorbed X-ray spectra (see e.g. Mainieri et al. 2002; Kim et al. 2004).
We conclude that there is a larger fraction of OFS with flat X-ray spectral slopes. To confirm that this flattening is due to high intrinsic absorption we fit the X-ray spectra of each source. We discuss this in more detail in §7.

[1] The HR is a reasonable indicator of the intrinsic column density of an AGN only for $z \lesssim 1.5$. At higher redshifts an absorbed AGN can have a lower HR value due to the higher rest-frame energies probed in the observed X-ray band.

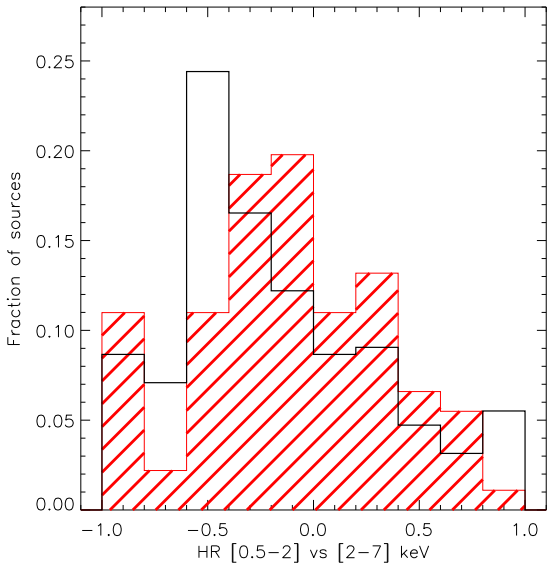

Fig. 4. The distribution of hardness ratios (HR) for the optically faint sample (hatched histogram) and the optically bright sample (open histogram).

4. Photometric redshift technique applied to an X-ray selected sample

Given the optically faintness of the OFS, the only viable way to determine their redshifts is to use photometric redshift techniques. In recent years, these techniques have achieved good accuracy, particularly when high quality multiwavelength imaging data is available; e.g. $\sigma_z = 0.06(1 + z)$ for the *Hubble* Deep Field North (Fernández-Soto et al. 1999; Benitez 2000; Furusawa et al. 2000). These procedures rely on detecting the passage of continuum features within the spectral energy distribution (SED) of sources across a series of photometric passbands (e.g., the 4000Å break).

Recently these techniques have also been applied to the optical counterparts of X-ray sources. For these sources the contribution to the optical/near-IR emission from the AGN nucleus can be significant. Gonzalez & Maccarone (2002) studied a sample of 65 sources detected by *Chandra* in the *Hubble* Deep Field North and flanking fields. By using a set of galaxy templates, and excluding objects dominated by the emission from the QSO, they were able to obtain photometric redshifts to an accuracy similar to that achieved for non-active galaxies. Mobasher et al. (2004) used the wide multiwavelength photometry from the Great Observatories Origins Deep Survey (GOODS)[2] to derive photometric redshifts for a sample of 19 AGN with spectroscopic identification. They found an *rms* scatter of ≈ 0.13, good enough to be useful for many science applications. Finally, Zheng et al. (2004), using the GOODS photometry, estimated photometric redshifts for the full sample of 346 X-ray sources detected in the CDF-S (Giacconi et al. 2002). By comparison with known spectroscopic redshifts (137 sources from Szokoly et al. 2004) we derived an average dispersion $\Delta z/(1 + z) \approx 0.08$.

In Zheng et al. (2004), we presented photometric redshifts for the full sample of X-ray sources in the CDF-S. In this work, we fully describe our methodology developed to produce the best results for the OFS. By determining likelihood contours in the *redshift* vs *template* plane, our approach clearly elucidate degeneracies/dependencies between redshift and SED/reddening which often affect the photometric redshift determination.

4.1. Multicolour catalogue

A key ingredient for deriving reliable photometric redshifts is broad, multi-wavelength coverage and accurate photometry. An area of ≈ 160 arcmin^2 of GOODS/CDF-S has been imaged with the Advance Camera for Surveys (ACS) on board of the Hubble Space Telescope (HST) in the F435W, F606W, F775W and F850LP bands (Giavalisco et al. 2004). A large program with the VLT is under way to image the GOODS area in the J, H, K_s bands, using some 32 ISAAC fields to mosaic a 150 arcmin^2 region (Vandame et al. in preparation)[3]; in addition, an extensive spectroscopic campaign has been completed with FORS2 at ESO (Vanzella et al. 2004) and additional spectroscopy with VIMOS is

[2] see: http://www.stsci.edu/science/goods/
[3] see: http://www.eso.org/science/goods/releases/20040430/

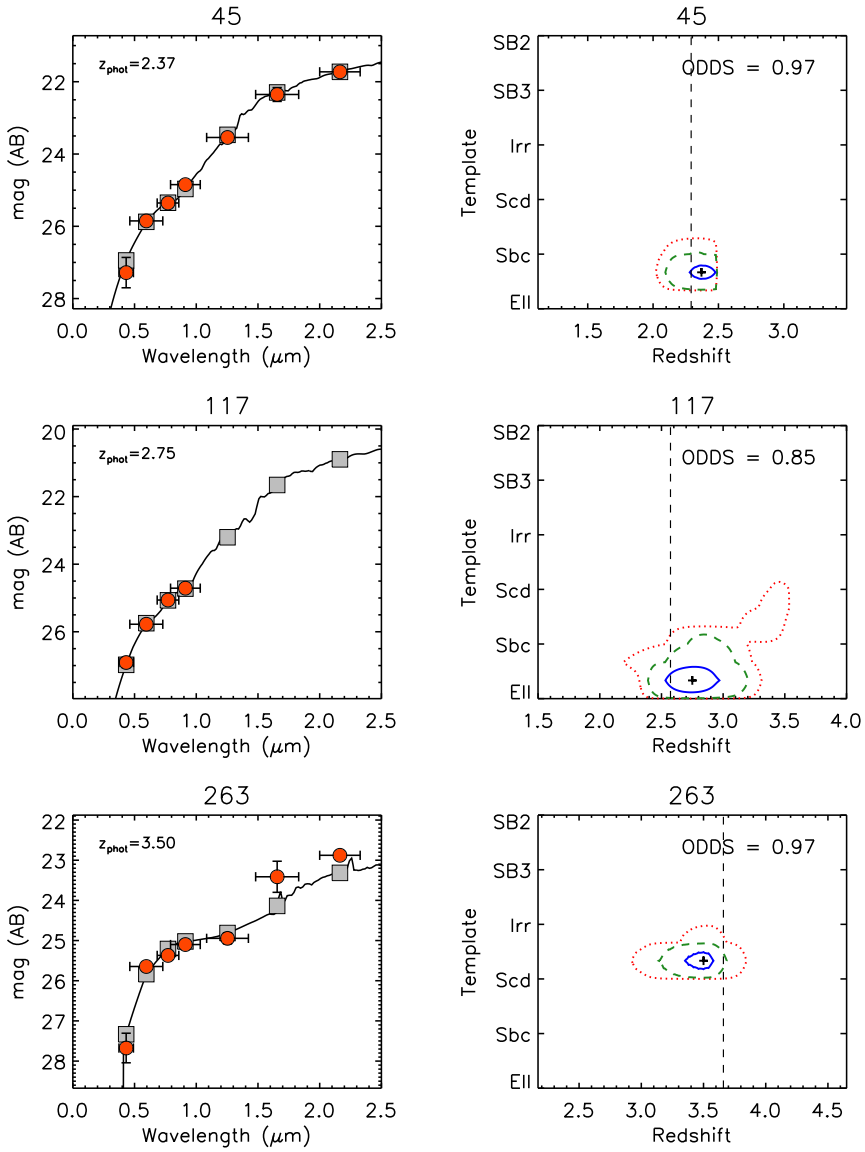

Fig. 5. Comparison of the photometric and spectroscopic redshifts of the spectroscopically identified OFS in the "GOODS area". *Left side*: best fit template (continuum line) with the observed photometry (filled circles with error bars) and the best fit model photometry (filled squares) overplotted. *Right side*: 1σ (dotted line), 2σ (dashed line) and 3σ (continuum line) confidence contours for the photometric redshift determination in the SED template *vs* redshift plane. The dashed line indicates the spectroscopic redshift and the cross shows the best fit solution. The shaded area refers to a low-probability region in the solution space (see Sec. 4.2). XID are from Giacconi et al. (2002).

planned in 2005.[4] The CDF-S has also been selected as one of the target fields in the Spitzer legacy program GOODS (Dickinson et al. 2002). For an overview of the available data in this field we refer the reader to Giavalisco et al. (2004).

We will restrict our photometric redshifts estimation only to the region of the CDF-S covered by deep HST/ACS imaging (see Figure 1) and we will refer to it as the *"GOODS area"*. In this region there are 192 X-ray sources, 112 of which have a spectroscopic redshift (Szokoly et al. 2004). For this sample we have built a multicolour catalogue in B_{435}, V_{606}, i_{775}, z_{850}, J, H, K_s bands. For the four optical bands we refer to the publicly available GOODS catalogue[5], while in the near-IR we use the deep VLT/ISAAC observations (Vandame et al. in preparation), when available, or the shallower NTT/SOFI imaging (Vandame et al. 2001).

We used SExtractor (Bertin & Arnouts, 1996) for source detection in each band. To obtain reliable source colours the spread in seeing conditions for images in different wavebands has been taken into account. We obtained PSF-matched

[4] see: http://www.eso.org/science/goods/
[5] http://www.stsci.edu/science/goods/

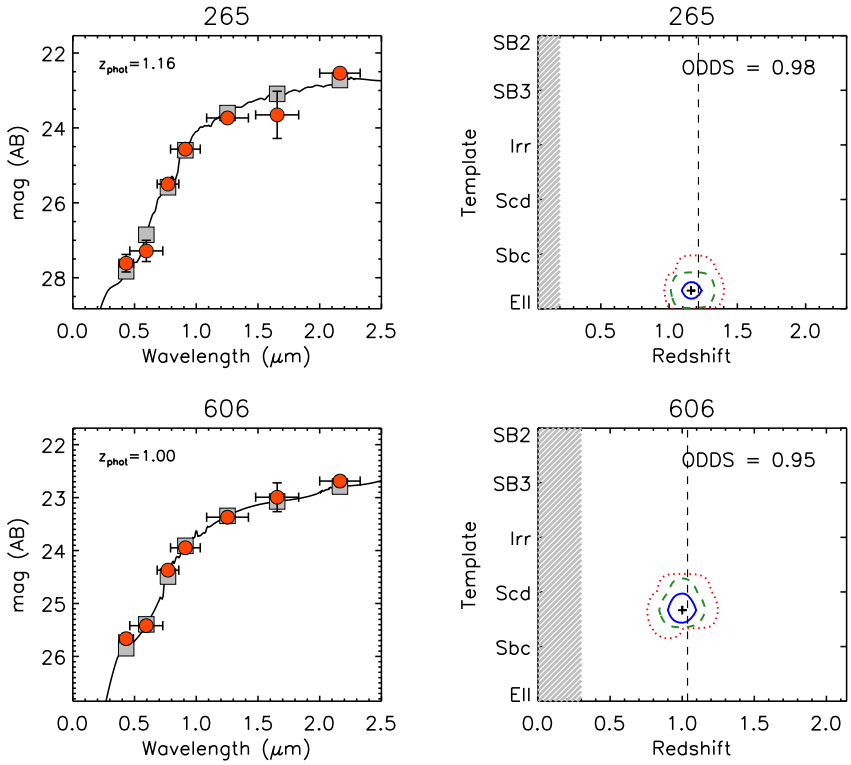

Fig. 6. As in Figure 5

magnitudes as follows: 1) we computed aperture magnitudes in each waveband using the available images ("original" images); 2) we degraded the point spread function (PSF) of each image to match the worst condition ("degraded" images); 3) we recomputed the aperture magnitudes using the "degraded" images; 4) we derived corrections for the different seeing conditions by comparing the magnitudes of "bright" stars in the "original" and in the "degraded" images. These corrections ($\lesssim 0.1$ mag) are applied to the "original" magnitudes. We checked that those corrections are constant over a large magnitude range. We also corrected for Galactic extinction: the values in the different filters have been obtained from the NASA/IPAC Extragalactic Database which are taken from Schlegel et al. (1998). The corrections in the CDF-S region are small (from ~ 0.03 mag in the B band to ~ 0.003 mag in the K_s band).

In the following, we adopt an X-ray based classification as suggested by Szokoly et al. (2004), but using unabsorbed luminosities and intrinsic absorption as opposed to uncorrected luminosities and hardness ratio (see Tozzi et al. 2005). We introduce the following classes: *X-ray unabsorbed QSO*: $L_X[0.5-10] \geq 10^{44}$ erg/s and $N_H < 10^{22}$ cm^{-2}; *X-ray unabsorbed AGN*: $10^{42} \leq L_X[0.5-10] < 10^{44}$ erg/s and $N_H < 10^{22}$ cm^{-2}; *X-ray absorbed QSO*: $L_X[0.5-10] \geq 10^{44}$ erg/s and $N_H \geq 10^{22}$ cm^{-2}; *X-ray absorbed AGN*: $10^{42} \leq L_X[0.5-10] < 10^{44}$ erg/s and $N_H \geq 10^{22}$ cm^{-2}; *galaxy*: $L_X[0.5-10] < 10^{42}$ erg/s and $N_H < 10^{22}$ cm^{-2}.

4.2. Photometric redshifts

Using the extraordinarily deep and wide photometric coverage in the "GOODS area", we have computed photometric redshifts for the OFS. This allows us to estimate the redshift distribution of OFS to a greater precision than has been performed before. For example, Alexander et al. (2001) assumed that most OFS reside in $\sim L^\star$ host galaxies to infer that the majority of the population is in the redshift range of $z \approx 1-3$.

We used the publicly available code BPZ (Benitez 2000)[6]. This code combines χ^2 minimization and Bayesian marginalization, using prior probabilities to include *a priori* knowledge of the distribution of galaxy magnitudes and spectral types with redshift. We used the default library of spectral templates in BPZ: four (E, Sbc, Scd, Irr) are spectral energy distributions from Coleman, Wu & Weedman (1980) and two are derived from spectra of starburst galaxies in Kinney at al. (1996). We allowed the code to calculate two interpolated SEDs between each pair of these templates. BPZ provides the "odds" parameter to characterize the accuracy of the redshift estimation. This parameter is defined as the integral of the redshift probability distribution within the interval $|z - z_b| < 2 \times \sigma(z)$, where z_b is the value

[6] BPZ is available from http://acs.pha.jhu.edu/~txitxo/

Table 1. Photometric redshifts for Optically Faint Sources in CDF-S/GOODS

XID[a]	R mag (Vega)	z_{spec}	z_{phot}	1 σ[b]	template[c]	odds[d]	X/O[e]	N_H[f]	L_X[g] ([0.5 − 10] keV)	Class X[h]
45	25.4	2.291	2.37	2.23-2.43	1.67	0.97	23.8	$22.91^{23.05}_{22.74}$	44.18	QSO abs
58	26.0	...	0.92	0.75-1.07	2.00	0.60	19.2	$22.40^{22.49}_{22.31}$	43.16	AGN abs
79	26.5	...	2.00	1.91-2.07	1.00	0.98	36.4	<21.75	43.67	AGN unabs
79A*	26.5	...	1.82	1.76-1.86	1.33	1.00	36.4	<21.75	43.67	AGN unabs
81	26.0	...	2.59	2.47-2.59	2.33	0.95	10.2	$22.63^{22.86}_{22.26}$	43.81	AGN abs
82	25.9	...	1.89	1.79-1.97	1.33	0.97	12.1	$23.47^{23.52}_{23.42}$	43.79	AGN abs
108	25.9	...	1.56	1.48-1.66	2.33	0.96	8.4	$21.79^{22.28}_{19.90}$	43.15	AGN unabs
117	25.5	2.573	2.75	2.50-3.00	1.33	0.85	8.5	$22.49^{22.70}_{22.16}$	43.99	AGN abs
124	25.3	...	0.61	0.45-0.77	3.00	0.53	0.3	<21.62	41.75	galaxy
133	99.0	...	1.21	0.78-4.08	2.00	0.11	21.9	$22.75^{22.85}_{22.66}$	43.32	AGN abs
146	99.0	...	2.67	2.55-2.66	1.67	0.97	42.3	>24.18	45.11	QSO abs
147	25.1	...	0.99	0.89-1.10	2.00	0.87	16.3	$23.39^{23.45}_{23.33}$	43.67	AGN abs
148	27.3	...	1.74	1.62-1.88	1.67	0.87	69.9	>24.18	45.09	QSO abs
159	99.0	...	3.30	3.17-3.46	3.67	0.98	142.8	$23.00^{23.11}_{22.88}$	44.81	QSO abs
178	26.0	...	0.29	0.23-3.54	3.67	0.32	0.7	$21.68^{22.02}_{20.52}$	41.00	galaxy
210	99.0	...	1.73	1.60-1.95	1.33	0.74	18.1	$22.32^{22.56}_{21.87}$	43.36	AGN abs
217	25.8	...	7.72	1.08-7.62	5.00	0.30	0.8	$23.06^{23.31}_{22.61}$	43.80	AGN abs
221	99.0	...	2.51	2.34-2.62	1.00	0.90	1.6	$22.58^{23.00}_{21.08}$	43.32	AGN abs
226	99.0	...	1.45	1.14-1.87	5.67	0.39	24.4	$22.17^{22.35}_{21.88}$	43.35	AGN abs
227	99.0	...	2.18	1.98-2.36	1.33	0.77	33.8	$23.83^{23.91}_{23.74}$	44.24	QSO abs
240	25.0	...	1.41	1.35-1.53	1.33	0.95	4.4	$22.42^{22.62}_{22.22}$	43.13	AGN abs
243	99.0	...	7.89	7.56-7.93	4.00	0.99	40.2	$23.26^{23.36}_{23.16}$	44.11	QSO abs
263	25.3	3.660	3.50	3.32-3.56	3.33	0.97	5.5	>24.18	44.54	QSO abs
265	99.0	1.215	1.16	1.09-1.24	1.33	0.98	51.2	$23.20^{23.27}_{23.13}$	43.70	AGN abs
508	99.0	...	2.50	1.90-2.85	1.00	0.58	18.8	$23.88^{23.97}_{23.79}$	44.15	QSO abs

[a] XID from Giacconi et al. (2002).
[b] 1 σ confidence range.
[c] Best fit template. BPZ performs two interpolations between each one of the following templates:
1: Elliptical (CWW)
2: Sbc (CWW)
3: Scd (CWW)
4: Irregular (CWW)
5: SB3 (Kinney)
6: SB2 (Kinney).
[d] Odds parameter which gives a metric on the reliability of the photometric redshift determination (see Sec. 4.2).
[e] X-ray-to-optical flux ratios.
[f] Logaritm of the column density.
[g] Logaritm of the unabsorbed X-ray luminosity in the [0.5-10] keV band. The uncertainties are smaller than 0.01 in the adopted units.
[h] X-ray classification (see Sec. 4.1).
* Photometric redshift obtained using the UDF photometry (see Sec. 9 and Fig. 12,13).

which maximizes the probability distribution and $\sigma(z)$ the observed *rms*. A low value (< 0.6) of the odds parameter is a warning that the probability distribution is spread over a large redshift range or is double-peaked.

The reliability of the OFS photometric redshifts was estimated using the five spectroscopically identified OFS in the "GOODS area": CDF-S/XID 45, 117, 263, 265 and 606 (see Table 3 and Figure 5-6). In the left column the best fit template is plotted together with the observed photometry. On the right column, likelihood contours (1σ, 2σ, 3σ) are reported in the *SED template vs redshift* plane. In all of the five cases the agreement between the photometric and spectroscopic redshift is extremely good, even for source CDF-S/XID 117 for which we do not have reliable near-IR photometry. Therefore we are confident that we can apply this procedure to the whole of OFS class. In Table 1 and 2 we report the derived photometric redshifts and the 1 σ confidence range. Best fits and confidence contours for each source are shown in Figure 14.

We have also used X-ray information to set a posteriori constraints in the redshift solution space. In a plot of the Hardness Ratio *versus* the X-ray luminosity of the sources in the CDF-S (see Figure 10 of Szokoly et al. 2004) almost all of the sources spectroscopically identified as AGN have: HR> -0.6 and $L_X[0.5-10\ keV] > 10^{41.5}$ erg s^{-1}. Consequently for all the objects with HR> -0.6 we have imposed a minimum X-ray luminosity limit ($L_X^{\rm min}[0.5-10\ keV] = 10^{41.5}$ erg s^{-1}) that converts to a minimum redshift for each source ($z_{\rm min}$). In the confidence contour plots the shaded area

Table 2. Photometric redshifts for Optically Faint Sources in CDF-S/GOODS

XID[a]	R mag (Vega)	z_{spec}	z_{phot}	1 σ[b]	template[c]	odds[d]	X/O[e]	N_H[f]	L_X[g] ([0.5 − 10] keV)	Class X[h]
510	25.4	...	2.51	2.34-2.59	2.33	0.93	5.1	$23.44^{23.62}_{23.24}$	43.79	AGN abs
513	26.1	...	3.56	3.41-3.68	1.00	0.96	7.6	$24.16^{24.31}_{24.06}$	44.19	QSO abs
515	99.0	...	2.26	2.13-2.46	1.67	0.84	19.7	$23.50^{23.67}_{23.32}$	43.75	AGN abs
515*	99.0	...	2.30	2.24-2.38	2.00	1.00	19.7	$23.50^{23.67}_{23.32}$	43.75	AGN abs
518	99.0	...	0.84	0.58-1.37	2.00	0.33	9.5	$21.91^{22.31}_{20.68}$	42.23	AGN unabs
523	99.0	...	1.32	0.87-6.22	2.00	0.10	11.3	$22.98^{23.11}_{22.86}$	43.08	AGN abs
524	99.0	...	2.36	2.17-2.58	1.67	0.75	18.5	$23.39^{23.51}_{23.23}$	43.84	AGN abs
537	99.0	...	1.54	1.31-1.63	6.00	0.65	9.0	$22.62^{22.96}_{22.21}$	42.89	AGN abs
555	25.4	...	2.28	2.11-2.46	3.00	0.79	0.3	<22.68	42.83	AGN unabs
557	25.4	...	1.81	1.75-1.96	1.33	0.92	0.3	$22.66^{23.00}_{22.39}$	42.88	AGN abs
561	99.0	...	0.62	0.50-0.87	2.33	0.47	1.6	<21.38	41.82	galaxy
564	99.0	...	0.43	0.23-0.54	4.33	0.51	1.4	$21.79^{22.13}_{21.10}$	41.53	galaxy
572	27.0	...	2.73	2.21-2.68	2.00	0.53	1.8	$23.43^{23.68}_{23.17}$	43.62	AGN abs
583	99.0	...	2.77	2.66-2.88	1.00	1.00	2.2	$23.32^{23.49}_{23.11}$	43.77	AGN abs
589	99.0	...	1.33	0.89-6.51	2.00	0.10	1.2	$22.90^{23.11}_{22.57}$	42.81	AGN abs
593	25.9	...	2.07	1.83-2.15	2.67	0.77	0.6	$23.32^{23.61}_{22.95}$	43.31	AGN abs
599	25.2	...	2.84	2.48-2.82	1.33	0.76	1.9	$24.05^{24.17}_{23.92}$	43.99	AGN abs
605	99.0	...	4.71	4.39-4.83	5.00	0.85	8.2	$24.70^{24.93}_{24.49}$	44.52	QSO abs
605A*	99.0	...	4.29	4.21-4.32	3.67	0.99	8.2	$24.70^{24.93}_{24.49}$	44.52	QSO abs
606	25.3	1.037	1.00	0.92-1.06	2.67	0.95	4.8	$23.27^{23.40}_{23.14}$	43.16	AGN abs
610	99.0	...	2.04	1.94-2.17	1.00	0.90	8.7	>24.18	43.87	AGN abs
614	99.0	...	1.13	0.60-1.57	4.33	0.27	19.8	$21.30^{21.93}_{20.62}$	42.67	AGN unabs
618	25.6	...	4.66	4.59-4.72	6.00	1.00	0.8	$23.86^{24.10}_{23.75}$	44.30	QSO abs
626	25.4	...	0.59	0.55-0.62	6.00	1.00	0.4	$22.45^{22.89}_{21.25}$	42.94	AGN abs
628	99.0	...	2.07	2.01-2.17	2.00	0.99	1.2	$23.93^{23.95}_{23.93}$	43.68	AGN abs
629	25.3	...	0.56	0.49-0.61	6.00	0.97	0.3	<22.37	41.39	galaxy

corresponds to z< z_{min}, where the probability to have the correct solution is low (see Figure 5 and Figure 14).[7]
We compare in Figure 7 the redshift distribution of optically bright sources and OFS. We use the spectroscopic redshift, if known, or the derived photometric redshift, if the source is still unidentified. The solid histogram shows the redshift distribution of the OFS, the hatched histogram shows the distribution of optically bright sources, and the open histogram shows the distribution of the whole X-ray sample. We have excluded sources belonging to the two large scale structures at z = 0.67 and 0.73 discovered by Gilli et al. (2003) in the CDF-S. The uncertainties in the photometric redshifts are too large to determine whether a source belongs to these structures. Since 82% of the spectroscopically identified sources with $0.6 \leq z_{spec} \leq 0.8$ belong to the redshift spikes, we assumed that a similar fraction of sources with $0.6 \leq z_{phot} \leq 0.8$ are part of the same structures.

In Figure 7, we have overplotted for comparison the prediction of a synthesis model for the XRB [model B from Gilli, Salvati & Hasinger (2001)].

The majority of the OFS lie at z= 1 − 3, with a small fraction at z> 3, as previously predicted by Alexander et al. (2001). Perhaps surprisingly, a small fraction of OFS lie at z< 1. We note that a larger fraction (76%) of OFS are at z> 1 than found for the optically bright sources (49%). According to a K-S test the probability that these two distributions are drawn from the same population is extremely small ($\sim 0.00002\%$). These have to be taken into account when comparing the redshift distributions of recent deep *Chandra* and XMM-*Newton* surveys with XRB synthesis models predictions. Almost all of the spectroscopically identified sources in the two deepest *Chandra* pointings are optically bright: $\sim 97\%$ both in the CDF-S and CDF-N. It has been noted (Hasinger 2002; Gilli 2004) that the redshift distribution of these new surveys is in disagreement with XRB models predictions based on the ROSAT X-ray luminosity function. These models predict that the distribution peaks at z$\sim 1.3 - 1.5$, whereas the observed N(z) of the sources identified to date peaks at $z \lesssim 1$. Since OFS appear to have a N(z) peaking at z~ 1.7 (Figure 7) and they make up the majority of still unidentified sources, the disagreement with the models predictions is attenuated. Nevertheless, a significant discrepancy with the models remains even with the addition of photometric redshifts (Figure 7). A solution for this problem requires a new determination of the X-ray luminosity function of AGN (one of the main input parameters of XRB synthesis models), particularly exploring the X-ray fainter regime

[7] 99% of the X-ray sources in the CDF-S with spectroscopic redshifts and HR> −0.6 have $L_X[0.5 - 10\ keV] > L_X^{min}$

Table 3. OFS with a spectroscopic redshift in the CDF-S.

XID[a]	CXO CDFS[b]	R[c]	R−K[d]	z[e]	Q[f]	Opt[g]	X-ray[h]	FS[i]	FH[j]	HR[k]
45	J033225.8−274306	25.3	5.1	2.291	1	LEX	QSO abs	1.02 ± 0.08	4.67 ± 0.46	-0.12 ± 0.06
54	J033214.7−275422	25.7	<5.4	2.561	3	HEX	QSO abs	0.61 ± 0.07	3.37 ± 0.46	-0.01 ± 0.09
117	J033203.1−274450	25.5	4.9	2.573	3	HEX	AGN abs	0.61 ± 0.07	1.19 ± 0.34	-0.52 ± 0.11
263	J033218.9−275136	25.3	5.1	3.660	3	HEX	QSO abs	0.10 ± 0.04	1.23 ± 0.31	$+0.35 \pm 0.20$
265	J033233.4−274236	> 26	> 5.2	1.215[m]	1	LEX	AGN abs	0.19 ± 0.05	3.33 ± 0.45	$+0.50 \pm 0.11$
606	J033225.0−275009	25.3	4.3	1.037	1	LEX	AGN abs	< 0.06	1.25 ± 0.30	$+0.68 \pm 0.19$

[a] XID from Giacconi et al. (2002).
[b] IAU registered name, based on original X-ray coordinates.
[c] Vega R magnitude for the optical counterpart
[d] Vega R-K colour for the optical counterpart
[e] Optical spectroscopic redshift for the optical counterpart (Szokoly et al. 2004).
[f] Quality flag of the optical spectrum (see Szokoly et al. 2004).
[g] Optical classification (see Szokoly et al. 2004).
[h] X-ray classification.
[i] Flux in soft (0.5-2 keV) band, in units of 10^{-15} erg cm^{-2} s^{-1}.
[j] Flux in hard (2-10 keV) band, in units of 10^{-15} erg cm^{-2} s^{-1}.
[k] Hardness ratio, defined as (H−S)/(H+S) where H and S are the net counts in the hard and soft bands, respectively.

Table 4. X-ray spectral parameters of OFS with a spectroscopic redshift in the CDF-S.

XID[a]	CXO CDFS[b]	counts[c]	Γ[d]	N_H[e]	L_X[f]	cstat[g]
45	J033225.8−274306	302 ± 18	$1.46^{1.68}_{1.26}$	$22.91^{23.05}_{22.74}$	1.51×10^{44}	150.7
54	J033214.7−275422	186 ± 17	$1.38^{1.72}_{1.10}$	$23.03^{23.21}_{22.79}$	1.18×10^{44}	153.8
117	J033203.1−274450	136 ± 15	1.8	$22.49^{22.70}_{22.16}$	9.72×10^{43}	126.4
263	J033218.9−275136	46 ± 9	$1.75^{2.10}_{1.40}$	> 24.18	3.48×10^{44}	60.1
265	J033233.4−274236	114 ± 14	1.8	$23.20^{23.27}_{23.13}$	5.00×10^{43}	107.9
606	J033225.0−275009	33 ± 8	1.8	$23.27^{23.40}_{23.14}$	1.45×10^{43}	59.9

[a] XID from Giacconi et al. (2002).
[b] IAU registered name, based on original X-ray coordinates.
[c] Net counts in the [0.5-10] keV band.
[d] Spectral Index and 90% confidence range (Tozzi et al. (2005)).
[e] Logaritm of the intrinsic absorption (and 90% confidence range) [Tozzi et al. (2005)].
[f] X-ray luminosity in [0.5-10] keV band, deabsorbed and in erg s^{-1} [Tozzi et al. (2005)].
[g] C-statistic coefficient from the model fitting.

not covered by previous surveys (Gilli 2004). A similar result has been recently found by Fiore et al. (2003) using a different approach to derive the redshift information for unidentified sources in the HELLAS2XMM 1dF sample.

Finally, a significant fraction (46 out of 346, $\sim 13\%$) of the X-ray sources in the 1 Msec *Chandra* exposure (Giacconi et al. 2002), are not detected in deep VLT optical images down to $R \lesssim 26.1 - 26.7$. Yan et al. (2003) identified in the near-IR six of these objects using the first release of deep VLT/ISAAC JHK_s data, which covered an area 2.5 times smaller than the new extended ISAAC imaging shown in Figure 2. Using optical/near-IR colour-colour diagrams the authors concluded that they were likely to be E/S0 galaxies at $0 \leq z \leq 3.5$. Taking advantage of the deep optical ACS photometry we can now set tighter constraints on the redshift of these six sources: CDF-S/XID 201 has a spectroscopic redshift of z= 0.679 (Szokoly et al. 2004)[8]; the best fit SED of CDF-S/XID 79 and CDF-S/XID 221 is an unreddened early-type galaxy with redshift $1.82^{1.86}_{1.76}$ and $2.51^{2.62}_{2.34}$ respectively and the remaining three sources (XID/CDFS 515,561,593) are best fitted with the template of a spiral galaxy and have photometric redshifts of $2.30^{2.38}_{2.24}$, $0.62^{0.87}_{0.50}$ and $2.07^{2.15}_{1.83}$ respectively.

4.3. EXOs

The objects with extreme X-ray-to-optical ratios (EXOs) studied by Koekemoer et al. (2004) are also included in our sample. These sources were selected to be undetected in the ACS z band of the GOODS survey. In this work, by supplementing the HST imaging with new deep VLT/ISAAC data in J, H and K_s bands we can improve the photometric redshift accuracy. Since in several bands we have only upper limits, the confidence contours for these sources are

[8] This source is not reported in Table 3 and 1 because, as shown in Szokoly et al. (2004), an optical counterpart (201b) with R= 24.34 has been identified inside the *Chandra* error circle.

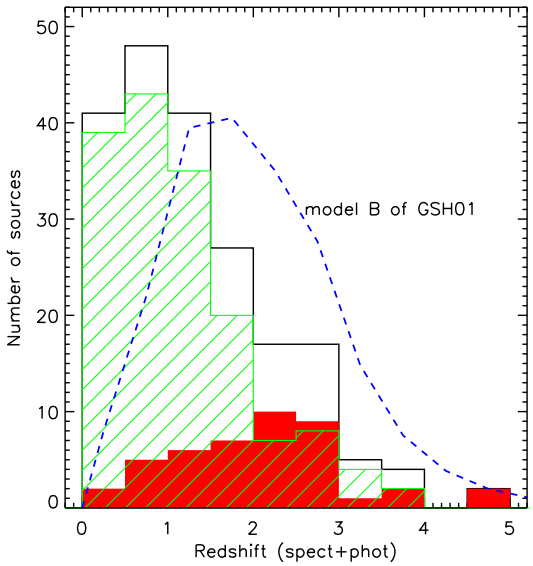

Fig. 7. Distribution of redshifts (spectroscopic and photometric) for the OFS (shaded histogram), optically bright sources (hatched histogram) and the total X-ray sample (open histogram). Sources belonging to the large scale structures in the CDF-S have been excluded (see text). The dashed line is the redshift distribution predicted by the model B of Gilli, Salvati and Hasinger (2001) normalized to the total number of sources in the "GOODS area" for which we have either a spectroscopic or photometric redshift.

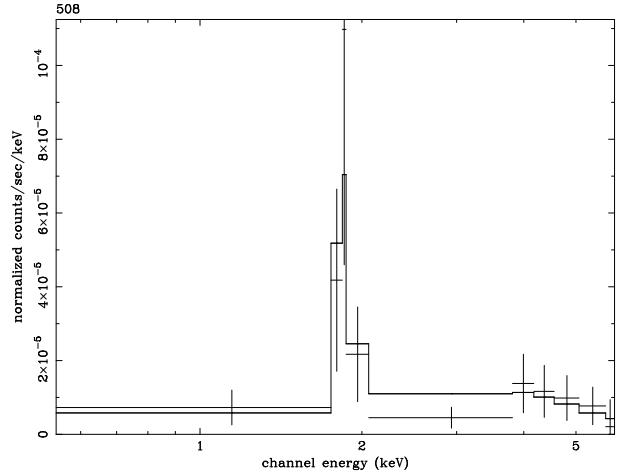

Fig. 8. X-ray spectrum of source CDF-S/508 with a significant feature that we identify with the Fe line at rest-frame 6.4 keV.

generally large and the low value of the odds parameter reflects the uncertainty in the redshift determination. However, in three cases we have odds$\gtrsim$0.6. The first, CDF-S/XID 243 has a single solution at high redshift ($z_{phot} \sim 7.9$, which gives an absorbed $L_X[0.5-10] = 2.0 \times 10^{45}$ erg s^{-1}, see Figure 14) and is best fitted with the SED of an irregular galaxy. Instead CDF-S/XID 508 has a double solution, with the peak of the redshift distribution corresponding at z$\sim$ 8.0 (absorbed $L_X[0.5-10] = 9.6 \times 10^{44}$ erg s^{-1}) but with a secondary peak at lower redshift ($\sim$ 2.4, absorbed $L_X[0.5-10] = 5.6 \times 10^{43}$ erg s^{-1}). We have inspected the X-ray spectrum of this source, and have detected a clear feature which, if identified with the Fe line at rest-frame 6.4 keV, would indicate a redshift of z$\simeq$ 2.5 (see Fig. 8). We therefore suspect that the lower redshift solution is correct. Finally, CDF-S/XID 583 is detected in the *v*, *i* and *z* ACS bands[9] and this favours a low redshift solution (z $\sim$ 2.7, absorbed $L_X[0.5-10] = 9.4 \times 10^{42}$ erg s^{-1}). These results do not exclude the high-redshift (z= 6 – 7) AGN scenario proposed by Koekemoer et al. (2004) for a small fraction of the EXOs population. We conclude that using the best multiwavelength imaging data set available to date, we have found

[9] In Koekemoer et al. (2004) only 3/5 of the ACS observation time were considered while here we have used the entire ACS data set.

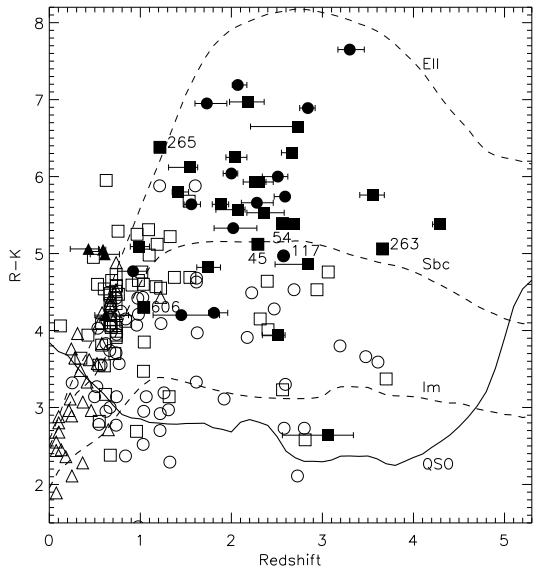

Fig. 9. R−K colour versus redshift. Following the X-ray classification (Szokoly et al. 2004) described in §4.1: circles are X-ray unabsorbed AGN/QSOs, squares X-ray absorbed AGN/QSOs, triangles galaxies. Filled symbols refer to OFS, empty symbols to optically bright sources. The numbers are the XIDs of OFS spectroscopically identified in the CDF-S (see Table 3). The four evolutionary tracks correspond to an unreddened QSO [solid line; Vanden Berk et al. (2001)], and to unreddened elliptical, Sbc and irregular galaxies from the Coleman, Wu & Weedman (1980) template library (dashed lines). The bars indicate 1 σ errors in the photometric redshift estimates.

a candidate at z$\geq$ 7; the other two EXOs are most likely at lower redshifts (z$\sim$ 2.5). Forthcoming Spitzer observations of this field shall determine more accurate photometric redshifts for the EXO population.

5. The properties of OFS with spectroscopic redshifts

For the few OFS with known redshifts, we can study their X-ray spectral properties. In the CDF-S, there are six of these objects and we report in Table 3 their main X-ray and optical properties. The depth of the 1 Msec CDF-S data enables us to perform an X-ray spectral analysis of these sources. We adopt a power-law model plus an absorption component. The fit yields the power-law photon index Γ, the intrinsic column density N_H, and the X-ray luminosity in the [0.5-10] keV rest-frame band corrected for absorption. We give the results of these fits in Table 4. Adopting the X-ray classification presented in Section 4.1, the sample comprises three X-ray absorbed QSOs, and three X-ray absorbed AGNs.

The identified OFS show a variety of optical classes in Table 3. Following the optical classification introduced by Szokoly et al. (2004)[10], there are: three objects showing high excitation narrow lines (C IVλ1549) together with narrow Lyα emission (HEX), CDF-S/XID 54,117,263, and three objects showing only low excitation lines (LEX) either Lyα, CDF-S/XID 45, or [O II]λ3727, CDF-S/XID 265,606. For the sources in the LEX class, the presence of an AGN is only revealed by their high X-ray luminosities.

In strongly absorbed X-ray sources, the host galaxy dominates the optical and near-IR emission. The R−K versus z diagram can be used to contrain the nature of the X-ray sources. We present this diagram in Figure 9 for all of the CDF-S sources with spectroscopic redshifts, highlighting the OFS. For comparison, we also plot the evolutionary tracks expected for classical Type-1 QSOs and galaxies of various morphological types. The optically faint X-ray population has on average redder colours than the optically bright population. For the 92 OFS of our sample, we find that 60 ($\sim$ 65%) of them are Extremely Red Objects (EROs), R−K$\geq$5, as compared to only 28 ($\sim$ 11%) for the optically bright population (see also Alexander et al. 2001 and 2002). The OFS with spectroscopic identification cover a wide redshift range (z= 1 − 4).

In Figure 9, we plot also the OFS for which we have determined a photometric redshift. Almost all of them have colours dominated by the host galaxy (elliptical or spiral) and, except for a few candidates at high redshift, the bulk of them lie in the redshift range of $1.5 \lesssim z \lesssim 2.5$, filling in a region that is poorly sampled by spectroscopically identified X-ray sources.

[10] The spectroscopic data of the CDF-S are publicly available at this URL: http://www.mpe.mpg.de/∼mainieri/cdfs_pub/

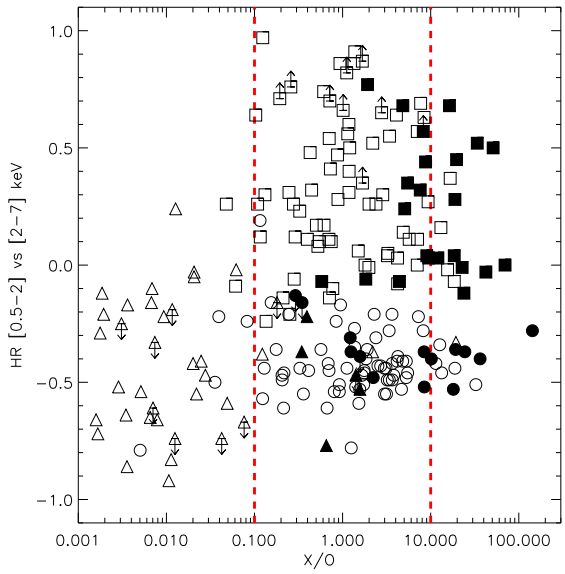

Fig. 10. The Hardness ratios (HR) versus X-ray-to-optical flux ratios (X/O). Open symbols indicate ptically bright (R< 25) sources and filled symbols indicate OFS. Symbols are as in Figure 9. For clarity, we have omitted optically bright objects that are spectroscopically unidientified. Vertical lines are for X/O= 0.1 and X/O= 10 respectively.

6. X-ray-to-optical flux ratios

X-ray-to-optical flux ratios (X/O) can yield important information on the nature of X-ray sources (Maccacaro et al. 1988). A value of $0.1 < X/O < 10$ is a clear sign of AGN activity since normal galaxies and stars usually have lower X-ray-to-optical flux ratios. In Figure 10, we show the hardness ratios (HR) versus X/O for the X-ray sources in the CDF-S area. The majority of X-ray unabsorbed and X-ray absorbed AGN/QSOs are inside the well defined locus of active galactic nuclei ($0.1 < X/O < 10$), while "normal" galaxies, for which the contribution to the X-ray flux is mainly due to star-formation activity, have X/O< 0.1. The OFS have ratios characteristic of AGN and $\sim$ 49% of them show intriguingly high values (X/O> 10).[11] In the spectroscopic follow-up of the CDF-S, three of the OFS with high X/O have been identified (Szokoly et al. 2004; Vanzella et al. 2004): CDF-S/XID 45,54 and 265 have redshifts of z= 2.291,2.561 and 1.215, respectively. Two of them are classified as X-ray absorbed QSOs and one as X-ray absorbed AGN (see Table 3). Recently, Mignoli et al. (2004) have studied a sample of eleven hard X-ray selected sources with X/O> 10 using deep near-IR observations with ISAAC. All but one of the sources have been detected in the K_S band with very red colors ($R-K_S > 5$). They were able to provide a morphological classification and the sample is dominated by elliptical profiles (7/10). Using the morphological information and the R−K colour the authors determined a minimum redshift for the sources in the range $z_{min} = 0.80 - 1.45$. In the OFS inside the "GOODS area" there are 20 objects with such high X/O values and we have determined photometric redshifts for them. Three sources (CDF-S/XID 133,523,614) have extremely low value of the odds parameter and we will exclude them in the following analysis. Two different classes of objects are present. Twelve ($\sim$ 71%) have a best fitting SED of an elliptical galaxy, the average column density is $\sim 1.0 \times 10^{23}$ cm^{-2} and their predicted redshift range is $0.9 < z_{phot} < 2.7$ (with a mean redshift of $\sim$ 1.9). The remaining sources have a best fitting SED of either an irregular or starburst galaxy, with a mean redshift of z$\sim$ 4 and X-ray spectra indicating a low value of absorption ($< N_H > \sim 1 \times 10^{22}$ cm^{-2}). One of these sources is the z> 7 candidate (CDF-S/XID 243) .[12]

Summarizing, $\sim$ 71% of the OFS with X/O> 10 are X-ray absorbed AGN and their photometry is well reproduced by an unreddened early-type template at $0.9 < z < 2.7$. The other 29% of the sources do not show strong X-ray absorption, they have bluer colours and among them there are some high redshift X-ray unabsorbed/absorbed QSOs. Finally, a significant fraction ($\sim$ 24%) of the sources with high X/O are X-ray absorbed QSOs.

[11] We note that $\sim$ 75% of the X-ray sources in the CDF-S with X/O> 10 are OFS.

[12] We are sampling an X-ray flux regime ($8 \times 10^{-16} \lesssim F_X[2-10\ \mathrm{keV}] \lesssim 7 \times 10^{-15}$ erg cm^{-2} s^{-1}) much fainter than the one studied by Mignoli et al. (2004), $1 \times 10^{-14} \lesssim F_X[2-10\ \mathrm{keV}] \lesssim 1 \times 10^{-13}$ erg cm^{-2} s^{-1} (M. Brusa PhD thesis).

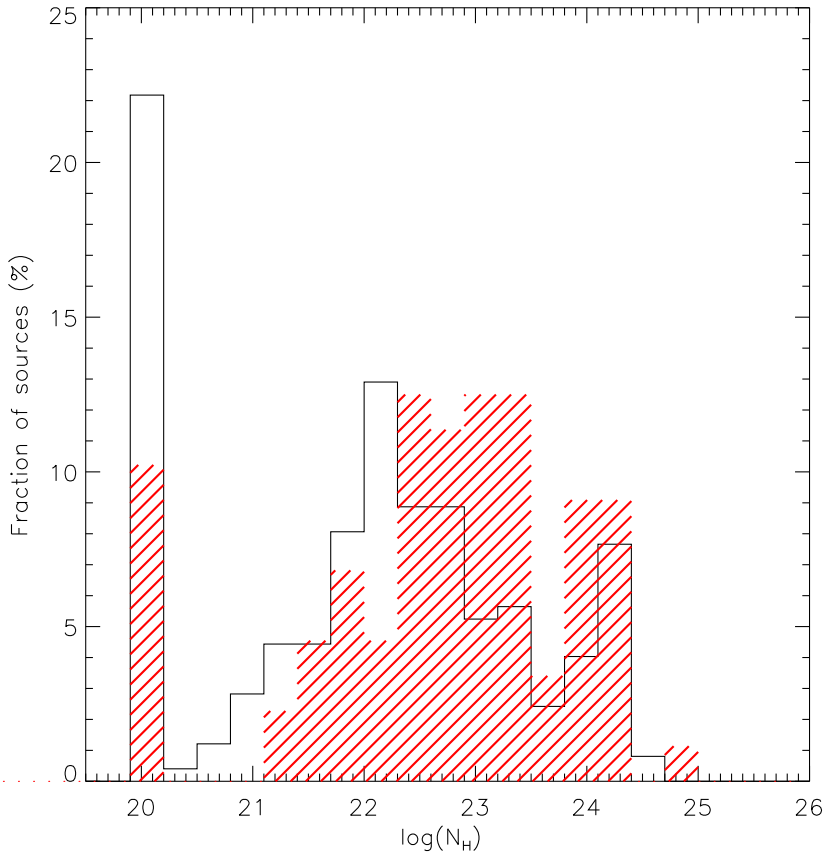

Fig. 11. Intrinsic N_H distributions for the OFS (hatched histogram) and optically bright sources (open histogram).

7. X-ray spectroscopy

To further investigate the characteristics of the OFS we have performed an X-ray spectral analysis of our sample. We use the X-ray data accumulated in the 1 Msec *Chandra* exposure and XSPEC (v11.1) for the fitting procedure. The spectral model adopted is a power-law with an intrinsic absorber at the source redshift. An additional photoelectric absorption component is fixed to the Galactic column density in the CDF-S region of the sky ($\sim 8 \times 10^{19}$ cm^{-2}). For sources with less than 100 net counts in the [0.5-10] keV band, we fix the photon index Γ at 1.8 and derive the column density N_H (see Tozzi et al. 2005). To estimate the intrinsic absorption that is affecting the X-ray source, its redshift is needed: we use the spectroscopic redshift if known otherwise we adopt the photometric redshift (Table 1). Thus, we are able to estimate the N_H value for 336[13] ($\sim$ 97%) of the 346 X-ray sources in the CDF-S. We show in Figure 11 the derived N_H distribution. The open histogram is the distribution for optically bright sources while the hatched histogram refers to OFS. A K-S test of the two distributions gives a probability of $\sim$ 0.004% that they are draw from the same population. We have already deduced from other diagnostics (X/O, hardness ratios, optical/near-IR colours) that a large fraction of these faint sources are absorbed. Figure 11 confirms and reinforces this picture since, in this case, we are measuring directly the absorption from the X-ray spectrum. Of the OFS $\sim$ 73% have a column density larger than 10^{22} cm^{-2}; for comparison the fraction of bright sources with such high N_H value is $\sim$ 55%. X-ray unabsorbed sources (the first bin in Figure 11) are approximatly three times more numerous between the optically bright than the optically faint sources.

8. X-ray absorbed QSOs

As mentioned in Section 5, a fraction of OFS could be made of X-ray absorbed QSOs. We find that 11 ($\sim$ 23%) of the OFS for which we have computed photometric redshifts have an X-ray luminosity in the [0.5-10] keV band larger than

[13] The remaining sources are either without a redshift estimate (four) or are stars (six).

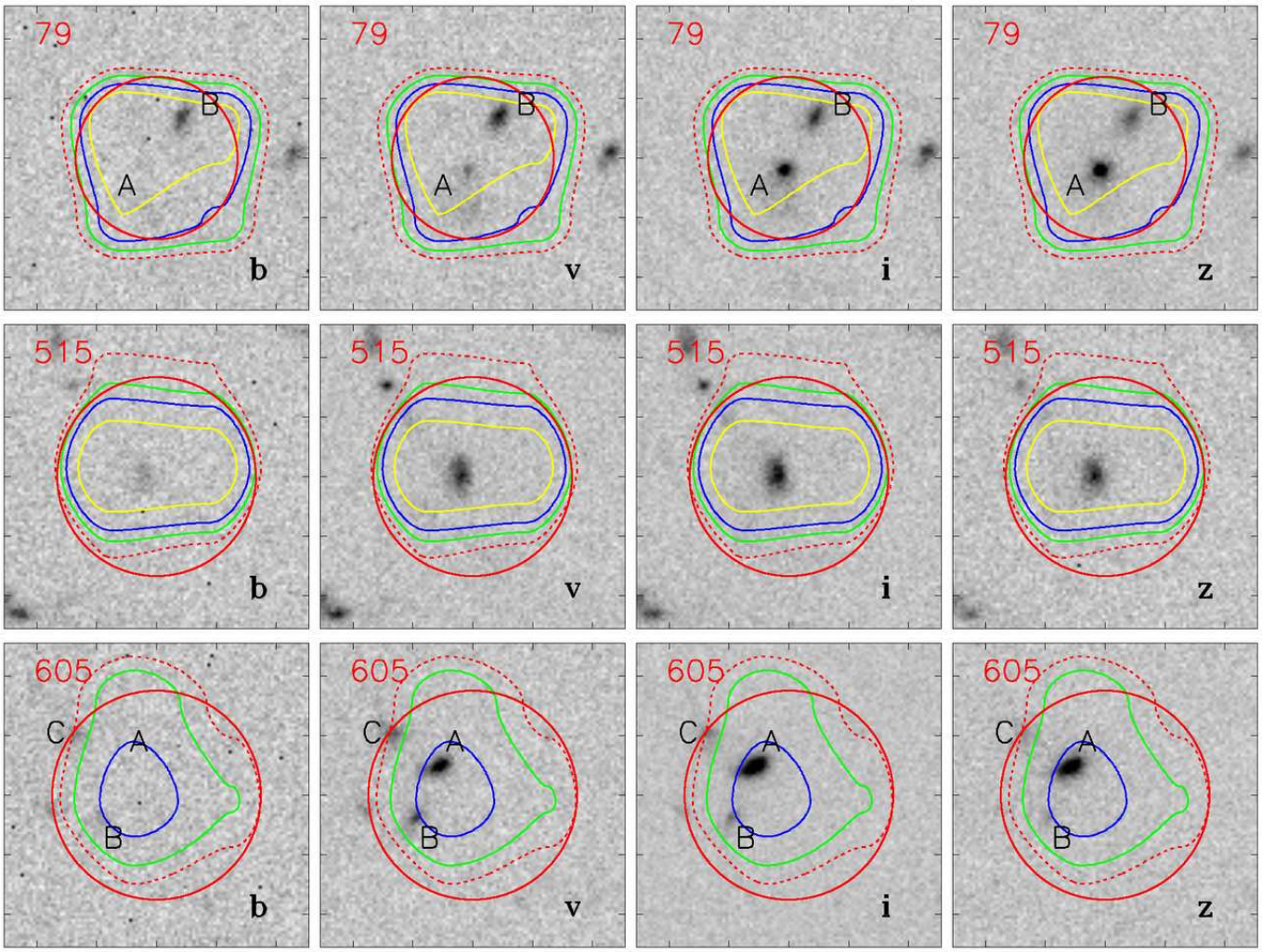

Fig. 12. Cutouts in the four UDF filters (F435W, F606W, F775W, F850LP) with X-ray contours of the three OFS inside this area. Images are 3″across. The 3σ *Chandra* positional error is indicated by the solid circle.

10^{44} erg s^{-1} and a $N_H > 10^{22}$ cm^{-2}, and consequently X-ray absorbed QSOs according to our definition in Section 4.1.

Several synthesis models of the XRB require a large population of obscured QSOs. To compare our results with the Gilli, Salvati & Hasinger (2001) and Ueda et al. (2003) models, we need to use the following definition of a X-ray absorbed QSO: rest-frame $L_X[2-10$ keV$] > 10^{44}$ erg s^{-1} and $N_H > 10^{22}$ cm^{-2}. We find that 44 sources of the 336 X-ray sources (optically bright and faint) for which we were able to determine N_H, satisfy these criteria. These X-ray absorbed QSOs contribute to the [2-10] keV XRB for a fraction of $\sim 15\%$ (if we adopt the HEAO-1 measure of the total flux of the XRB in the $[2-10]$ keV band)[14]. Model B of Gilli, Salvati & Hasinger (2001) predicts a 38% contribution from Type II QSOs to the hard XRB, while the recent model by Ueda et al. (2003) requires a lower contribution from these sources ($\sim 16\%$) in good agreement with what we have found.

9. Ultra Deep Field

The Hubble Ultra Deep Field (UDF) is a 400-orbit program to image one single field inside the 'GOODS area' with the ACS camera on board of HST (see Figure 1). Images have been taken in the same four filters that were used for the GOODS survey: F435W (b), F606W (v), F775W (i) and F850LP (z). The data have been recently released and go 1.0 and 1.2 magnitude deeper than GOODS in the b and z band, respectively.[15]

[14] We note that at the depth of the CDF-S survey the whole hard XRB has been resolved according to the HEAO-1 measure (Rosati et al. 2002).

[15] http://www.stsci.edu/hst/udf/

Inside the UDF area there are sixteen X-ray sources in the Giacconi et al. (2002) catalogue and three of them are OFS: CDFS/XID 79,515,605.[16] We have extracted cutouts for these faint sources in the four UDF bands and show them in Figure 12. The unprecedented depth and resolution of these images allows us to observe the optical properties of OFS with sub-arcsecond resolution. We indicate in the cutouts the 3 σ positional error circle obtained in Giacconi et al. (2002), which takes into account the strong effect of off-axis angle in the X-ray PSF and centroid. For CDFS/XID 79 two different counterparts are clearly present. We name these sources 79A and 79B (see Figure 12). They have different colours: 79A is undetected in the b band and is brighter than 79B in the i and z bands. In the cutouts of CDFS/XID 515 there is only one optical counterpart inside the Chandra error circle. Finally, for CDFS/XID 605 we find three optical counterparts (A, B, C) of which two are extremely faint in all four bands (B and C). We have selected from the publicly available catalogue of the UDF (h_udf_wfc_V1_cat.txt) source magnitudes in the four bands for each of the optical counterparts. The magnitudes available from this catalogue where computed using the i band isophotes of each source, thereby producing isophotally matched magnitudes that are suitable to compute colours. Combining these colours with our near-IR photometry, we estimated photometric redshifts as decribed in Section 4.2 (Figure 13). We provide individual notes on each source below.
Source CDFS/XID 79: the A counterpart is well fitted with an early-type SED at redshift $z_{phot} \sim 1.8$, similar to that obtained using the GOODS photometry (see Figure 14). However, we could not obtain a reasonable fit to source 79B, probably because the near-IR photometry (which does not resolve the two counterparts) is dominated by 79A.
Source CDFS/XID 515: we obtain $z_{phot} \sim 2.3$ and the confidence contours are in good agreement with the value found with the GOODS photometry (see Figure 14).
Source CDFS/XID 605: in this case the depth of the UDF data is really a step forward for the redshift determination. With the GOODS photometry we obtained a "double" solution with a peak in the probability distribution at low ($z_{phot} \sim 0.8$) and high ($z_{phot} \sim 4.7$) redshift (see Figure 14). With the UDF data we have smaller errors on the photometry and can put a more stringent upper limit in the b band where CDFS/XID 605 is undetected: this source is now a strong candidate at high redshift with $z_{phot} \sim 4.29$, with a small uncertainty $(4.21 - 4.32)$.

10. Conclusions

In this paper, we have taken advantage of the unique multi-wavelength coverage of the GOODS survey in the Chandra Deep Field South to constrain the nature and redshift distribution of optically faint X-ray sources (R$\geq$ 25). It is important to study their properties since they are a significant fraction ($\sim$ 27%) of the whole X-ray sample.
Our study extends the earlier analysis by Alexandet et al. (2001) by determining photometric redshifts for the optically faint sources without spectroscopic redshifts. The reliability of these photometric redshifts has been tested against the spectroscopic redshifts available for the optically faint fources (see Figure 5). We find that a larger fraction of the optically faint (76%) sources are at redshift $z > 1$ compared to the optically bright sample (49%). This finding reduces the disagreement between the observed redshift distribution in *Chandra* deep fields (Barger et al. 2003, Szokoly et al. 2004) and that predicted by XRB models based on the ROSAT X-ray luminosity function, as the majority of the still unidentified X-ray sources in these deep fields are optically faint. However, the redshift distribution that we obtain including our best photometric redshifts still peaks at $z \lesssim 1$, while the current XRB models predict $z \sim 1.3 - 1.5$. One solution would involve implementing a new X-ray luminosity function for AGN in the XRB synthesis models, by combining Deep *Chandra* and XMM-*Newton* fields with shallower surveys (Gilli et al. 2004; Fiore et al. 2003). This new X-ray luminosity function will be able to reproduce better the evolution with redshift of Seyfert-like objects which make a large fraction of the observed peak at $z \lesssim 1$.

Several diagnostics indicate that the majority of the optically faint sources are absorbed. Their hardness ratio distribution is harder (98% significance level) than that of the optically bright sample indicating a large fraction of optically faint fources with a flat X-ray spectrum which implies intrinsic absorption. Their optical/near-IR photometry is dominated by the emission of the host galaxies and their colours are in average redder that the optically bright sources [65% are EROs, (R-K$\geq$ 5) as compared to 11% of the optically bright sources]. We have performed an X-ray spectral analysis and the distribution of N_H values shows that $\sim$ 73% of OFS have column densities larger than 10^{22} cm^{-2} (for optically bright sources the fraction is of 55%).

We find that $\sim$ 23% of the optically faint X-ray sources are X-ray absorbed QSOs ($L_X[0.5 - 10\text{keV}] > 10^{44}$ erg s^{-1} and $N_H > 10^{22}$ cm^{-2}). Synthesis models of the XRB include a significant contribution from X-ray absorbed QSOs to the hard XRB (i.e. 38% for model B of Gilli, Salvati & Hasinger 2001). From the CDF-S survey we find a much lower contribution from obscured QSOs, $\sim$ 15%. This difference can not be ascribed to the remaining fraction of the as yet unresolved XRB: both the model and observational values are derived assuming the HEAO-1 measure of the total flux of the XRB in the $[2 - 10]$ keV band and the hard XRB has been resolved (using the HEAO-1 value) to the

[16] We have also checked the Alexander et al. (2003) catalogue, which includes all of the sixteen sources of Giacconi et al. (2002) plus one extra source with $\sim$ 12 counts in the full *Chandra* energy band and with an optically bright counterpart.

depth of the CDF-S (Rosati et al. 2002).
Our value is in good agreement with the prediction ($\sim 16\%$) based on the recent model by Ueda et al. (2003).

Approximatly 50% of the OFS have high X-ray-to-optical ratios (X/O$>$ 10). 71% of them are strongly X-ray absorbed ($<N_H> \approx 1.0 \times 10^{23}$ cm^{-2}) and their photometry is well reproduced by the SED of an early-type galaxy with $0.9 < z_{phot} < 2.7$. The remaining 29% is on average less absorbed ($<N_H> \approx 1 \times 10^{22}$ cm^{-2}) and has bluer colours reproduced by irregular or starburst galaxies with a mean redshift of ~ 4. Among this second group we find a candidate at redshift $z \gtrsim 7$. Finally, $\sim 24\%$ of the sources with high X-ray-to-optical ratios are X-ray absorbed QSOs.

Acknowledgements. We are grateful to Narciso Benitez for his assistance with BPZ. We thank the referee, B.J. Wilkes, for a very detailed and useful report that improved the manuscript. DMA thanks the Royal Society for financial support. CN gratefully acknowledge support under NASA grants NAG-8-1527 and NAG-8-1133.

References

Alexander, D.M., Brandt, W.N., Hornschemeier, A.E.,et al. 2001, AJ, 122, 2156
ALexander, D.M., Vignali, C., Bauer, F.E., et al. 2002, AJ, 123, 1149
Alexander, D.M., Bauer, F.E., Brandt, W.N., et al. 2003, AJ, 126, 539
Barger, A.J., Cowie, L.L., Trentham, N., et al. 1999, AJ, 117, 102
Barger, A.J., Cowie, L.L., Capak, P., et al. 2003, AJ, 126, 632
Benitez, N. 2000, ApJ, 536, 2000
Bertin, E., & Arnouts, S. 1996, A&A Supplement, 117, 393
Brandt, W.N., Alexander, D.M., Hornschemeier, A.E., et al. 2001, AJ, 122, 2810
Coleman, G.D., Wu, C.C., & Weedman, D.W. 1980, ApJS, 43, 393
De Luca, A., & Molendi, S. 2004, A&A, 419, 837
Dickinson, M. & Giavalisco, M.: 2002 Proc. of the Workshop, The Mass of Galaxies at Low and High Redshift, eds. R. Bender and A. Renzini, in press [astro-ph/0204213]
Fernández-Soto, A., Lanzetta, K.M., & Yahil, A. 1999, ApJ, 513, 34
Fabian, A.C., Smail, I., Iwasawa, K., et al. 2000, 315 , L8
Fiore, F., Brusa, M., Cocchia, F., et al. 2003, A&A, 409, 79
Furusawa, H., Shimasaku, K., Doi, M., et al. 2000, ApJ, 534, 624
Giacconi, R., Gursky, H., Paolini, F.R., Rossi, B.B. 1962, Phys.Rev.Letters, 9, 439
Giacconi, R., Zirm, A., Wang, J.X., et al. 2002, ApJS, 139, 369
Giavalisco, M., Ferguson, H.C., Koekemoer, A.M., et al. 2004, ApJL, 600, 93
Gilli, R., Salvati, M., & Hasinger, G. 2001, A&A, 366, 407
Gilli, R., Cimatti, A., Daddi, E., et al. 2003, ApJ, 592, 721
Gilli, R. 2004, Adv. Sp. Res., 34, 2470
Gonzalez, A.H. & Maccarone, T.J. 2002, ApJ, 581, 155
Hasinger, G., Altieri, B., Arnaud, M., et al. 2001, A&A 365, L45
Hasinger, G. 2002, Proceedings of the Symposium 'New Visions of the X-ray Universe in the XMM-Newton and Chandra Era', ESA SP-488, ed. F. Jansen, in press, astro-ph/0202430
Kim, D.W., Wilkes, B.J., Green, P.J., et al. 2004, ApJ, 600, 59
Kinney, A.L., Calzetti, D., Bohlin, R.C., et al. 1996, ApJ, 467, 38
Koekemoer, A.M., Alexander, D.M., Bauer, F.E., et al. 2004, ApJL, 600, 123
Maccacaro, T., Gioia, I.M., Wolter, A., et al. 1988, ApJ, 326, 680
Mainieri, V., Bergeron, J., Hasinger, G., et al. 2002, A&A, 393, 425
Marshall, F., et al. 1980, ApJ, 235, 4
Mignoli, M., Pozzetti, L., Comastri, A., et al. 2004, A&A, accepted (astro-ph/0401298)
Mobasher, B., Idzi, R., Benitez, N., et al. 2004, ApJL in press
Revnivtsev, M., Gilfanov, M., Johoda, K., Sunyaev, R. 2004, submitted to A&A [astro-ph/0412304]
Rosati, P., Tozzi, P., Giacconi, R., et al. 2002, ApJ, 566, 667
Schlegel, D.J., Finkbeiner D.P., Davis, M. 1998, ApJ, 500, 525
Szokoly, G.P., Bergeron, J., Hasinger, G., et al. 2004, ApJS, 155, 271
Tozzi, P., Rosati, P., Nonino, M., et al. 2001, ApJ, 562, 42
Tozzi, P., Gilli, R., Mainieri, V., et al. 2005, A&A submitted
Ueda, Y., Akiyama, M., Ohta, K., Miyaji, T. 2003, ApJ, 598, 886
Vandame, B., Olsen, L.H., Jorgensen, H.E., et al. 2001, astro-ph/0102300
Vanden Berk, D.E., Richards, G.T., Bauer, A., et al. 2001, AJ, 122, 549
Vanzella, E., Cristiani, S., Dickinson, M., et al. 2004, submitted to A&A, astro-ph/0406591
Vecchi, A., Molendi, S., Guainazzi, M., Fiore, F., & Parmar, A.N. 1999, A&A, 349, L73
Yan, H., Windhorst, R., Röttgering, H., et al. 2003, ApJ, 585, 67
Zheng, W., Mikles, V.J., Mainieri, V., et al. 2004, ApJS, 155, 73

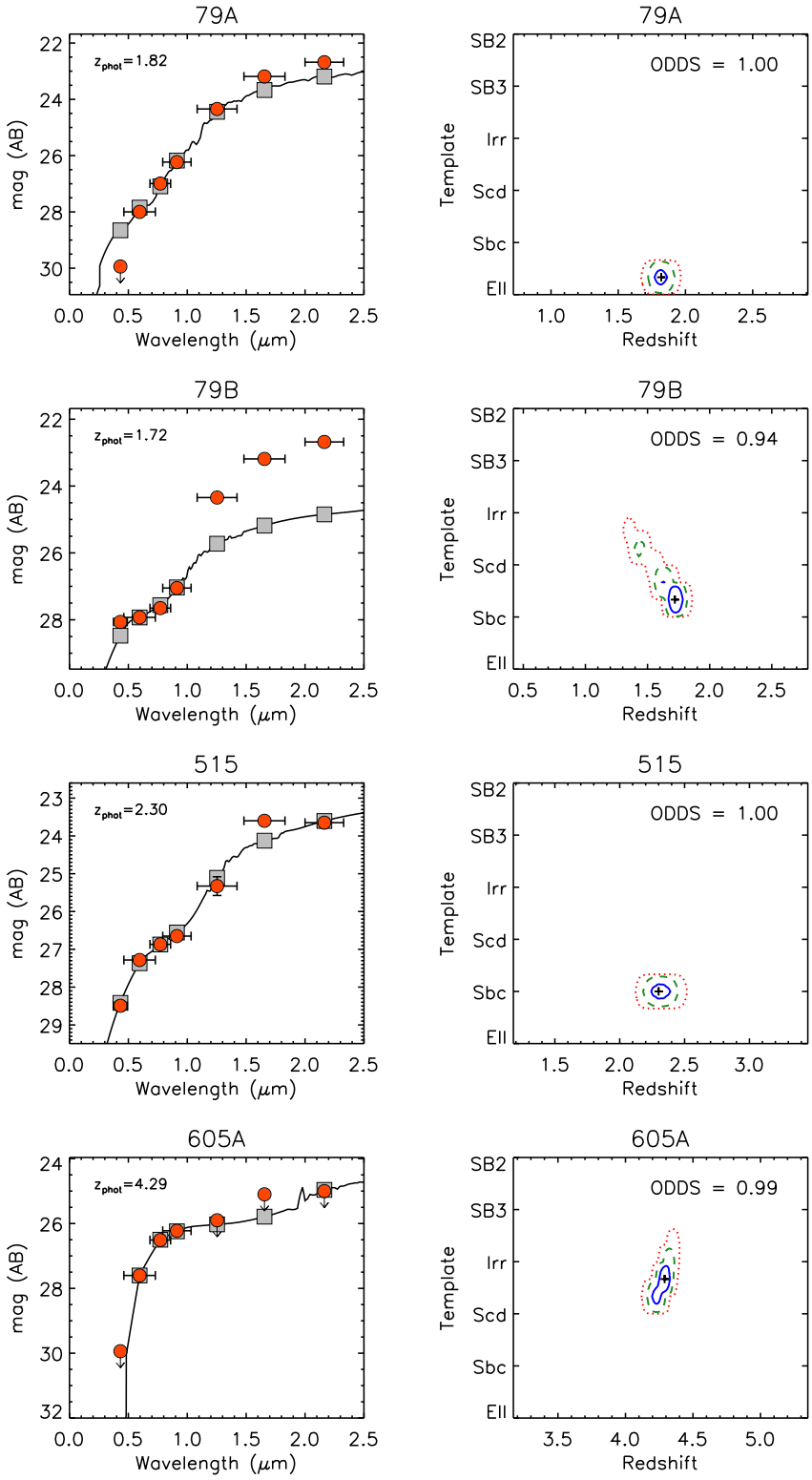

Fig. 13. Photometric redshifts for the counterparts of OFS in the UDF area. *Left side*: best fit template (solid line), the observed photometry (filled circles with error bars), and the best fit model photometry (filled squares). *Right side*: 1σ (dotted line), 2σ (dashed line) and 3σ (continuum line) confidence contours for the photometric redshift determination in the SED template *vs* redshift plane.

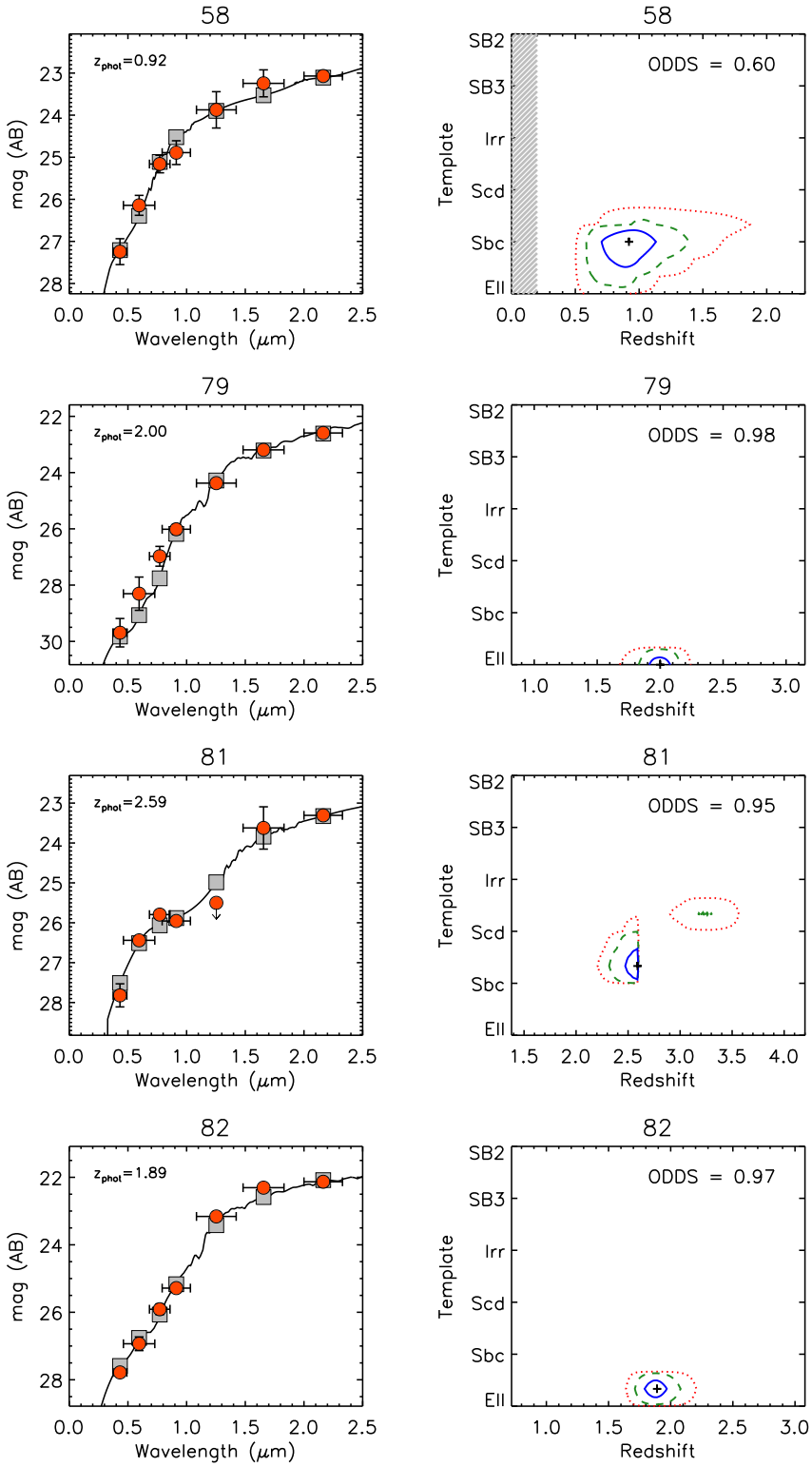

Fig. 14. Photometric redshifts for OFS in the "GOODS area" with odds$\geq$ 0.3. *Left side*: best fit galaxy template (solid line) with overplotted the observed photometry (filled circles with error bars), and the best fit model photometry (filled squares). *Right side*: 1σ (dotted line), 2σ (dashed line) and 3σ (continuum line) confidence contours for the photometric redshift determination in the SED template *vs* redshift plane. The cross indicates the best-fit solution. The shaded area refers to a low-probability region in the solution space (see text). The dot-dashed line for source 508 shows the redshift estimation based on the X-ray spectrum (see Sec. 4.3). XIDs are from Giacconi et al. (2002).

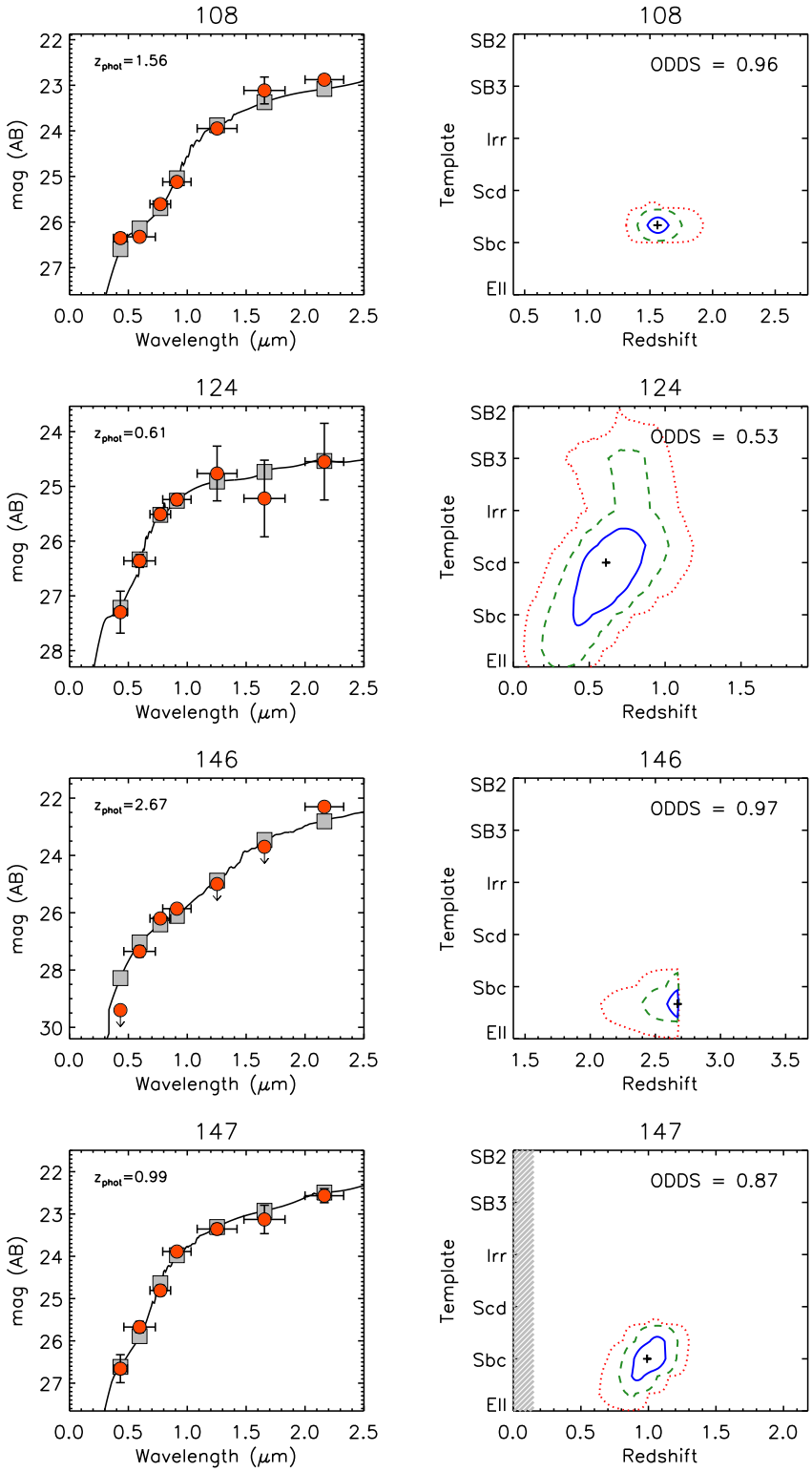
108
z_{phot}=1.56
mag (AB)
Wavelength (μm)
108
ODDS = 0.96
Template
SB2
SB3
Irr
Scd
Sbc
Ell
Redshift
124
z_{phot}=0.61
mag (AB)
Wavelength (μm)
124
ODDS = 0.53
Template
SB2
SB3
Irr
Scd
Sbc
Ell
Redshift
146
z_{phot}=2.67
mag (AB)
Wavelength (μm)
146
ODDS = 0.97
Template
SB2
SB3
Irr
Scd
Sbc
Ell
Redshift
147
z_{phot}=0.99
mag (AB)
Wavelength (μm)
147
ODDS = 0.87
Template
SB2
SB3
Irr
Scd
Sbc
Ell
Redshift

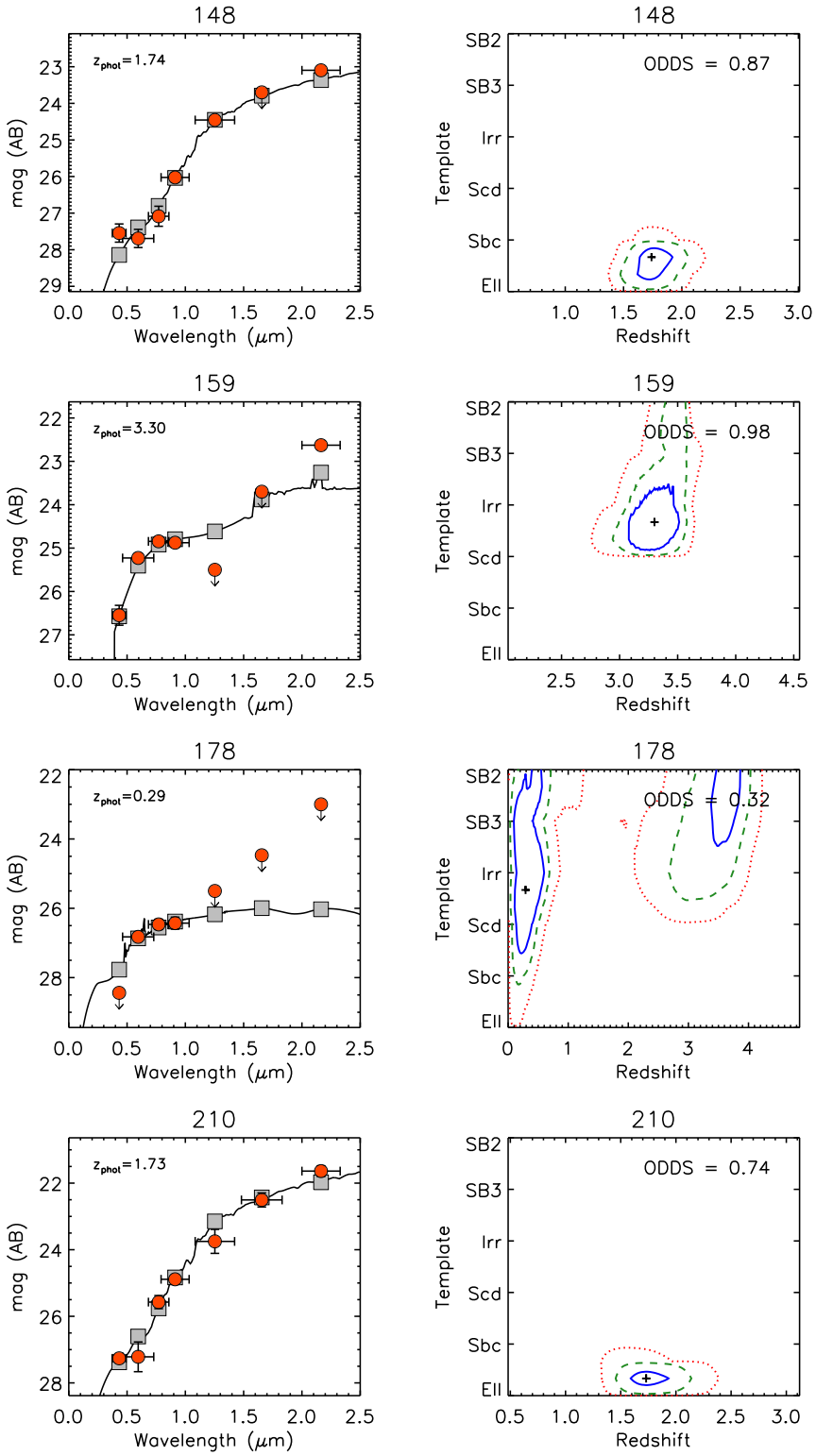
148
z_{phot}=1.74
mag (AB)
Wavelength (μm)
148
ODDS = 0.87
Template
SB2
SB3
Irr
Scd
Sbc
Ell
Redshift
159
z_{phot}=3.30
mag (AB)
Wavelength (μm)
159
ODDS = 0.98
Template
SB2
SB3
Irr
Scd
Sbc
Ell
Redshift
178
z_{phot}=0.29
mag (AB)
Wavelength (μm)
178
ODDS = 0.32
Template
SB2
SB3
Irr
Scd
Sbc
Ell
Redshift
210
z_{phot}=1.73
mag (AB)
Wavelength (μm)
210
ODDS = 0.74
Template
SB2
SB3
Irr
Scd
Sbc
Ell
Redshift

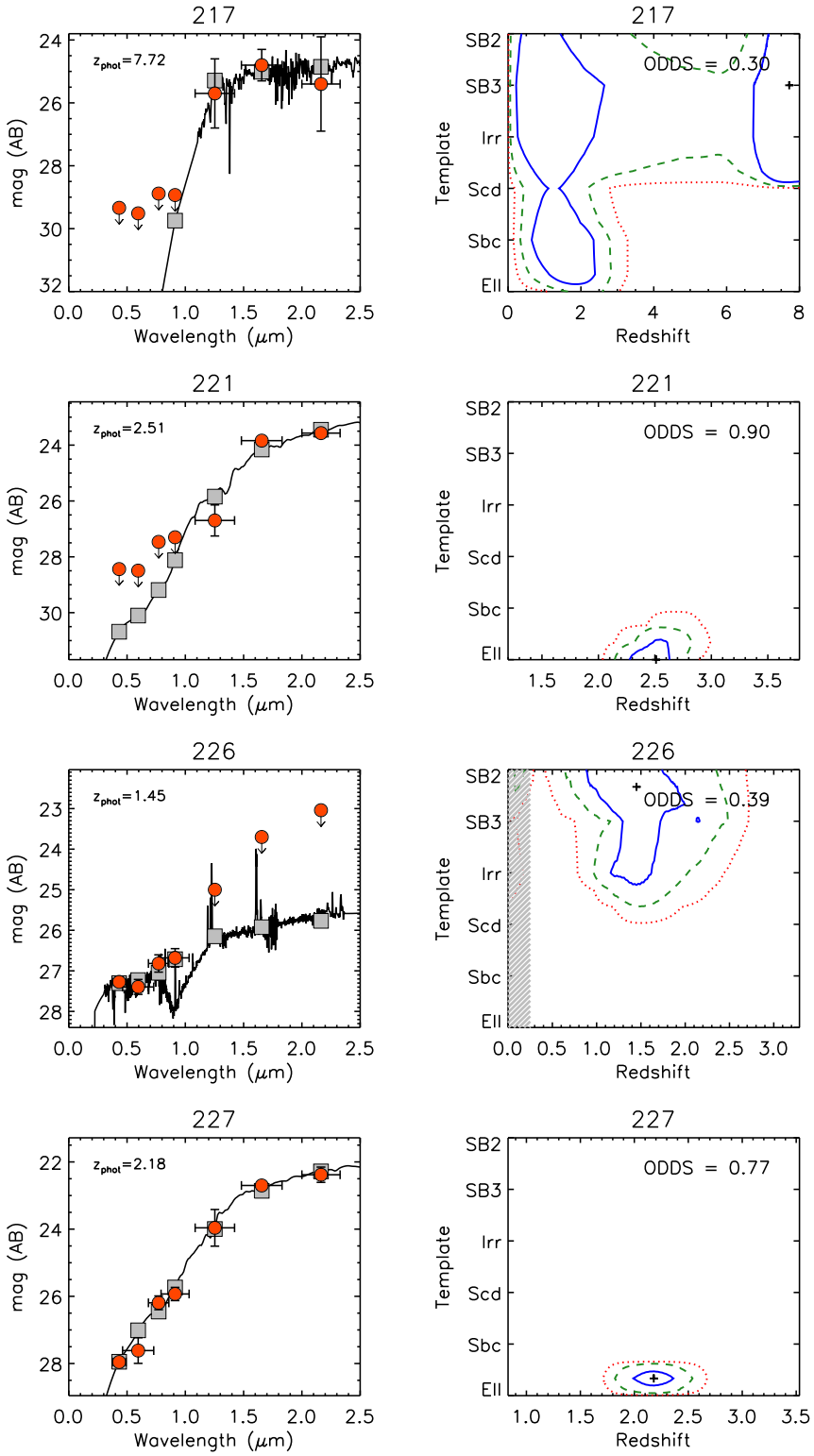
217
z_{phot}=7.72
mag (AB)
Wavelength (μm)
217
ODDS = 0.30
Template
SB2
SB3
Irr
Scd
Sbc
Ell
Redshift
221
z_{phot}=2.51
mag (AB)
Wavelength (μm)
221
ODDS = 0.90
Template
Redshift
226
z_{phot}=1.45
mag (AB)
Wavelength (μm)
226
ODDS = 0.39
Template
Redshift
227
z_{phot}=2.18
mag (AB)
Wavelength (μm)
227
ODDS = 0.77
Template
Redshift

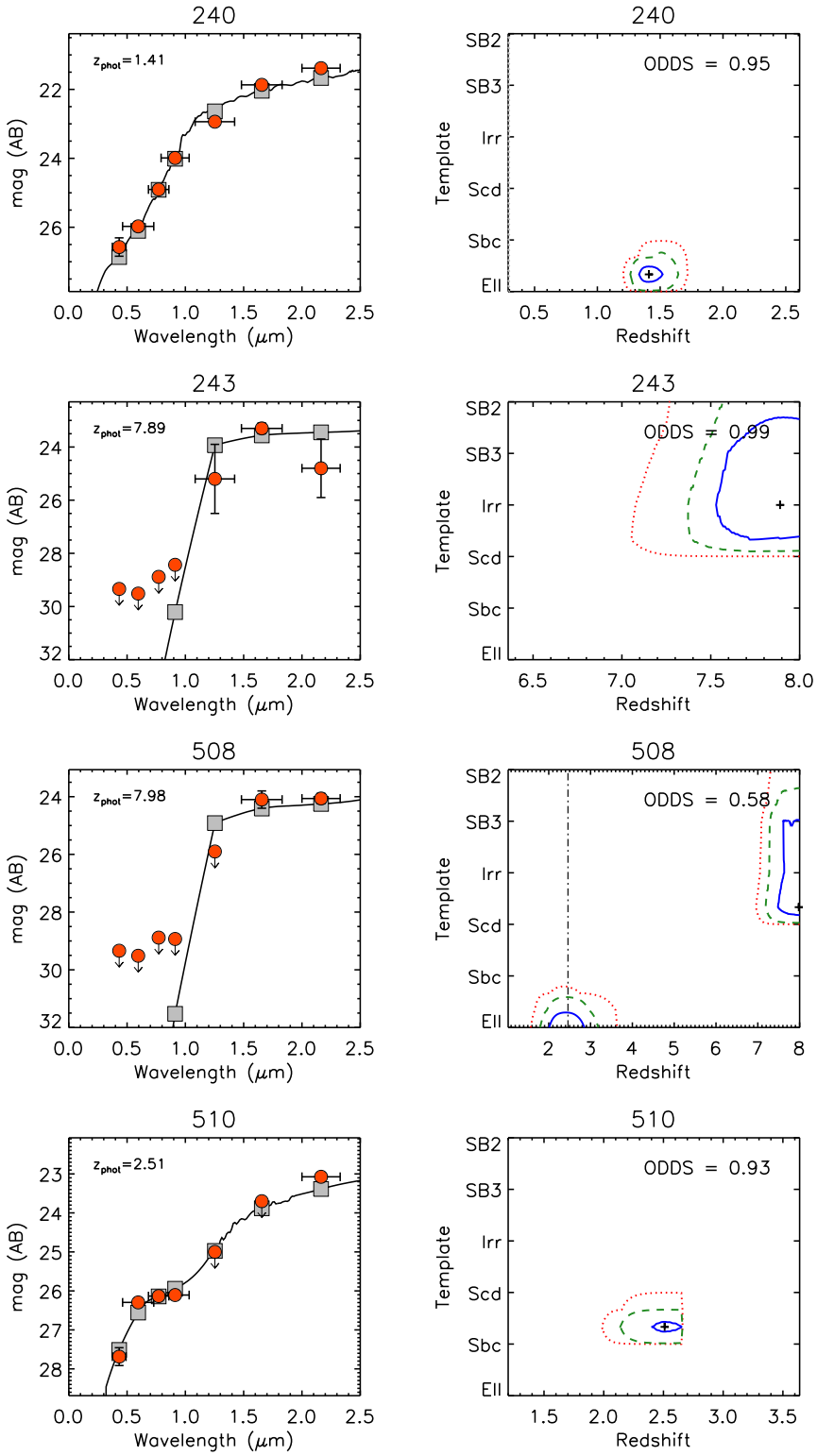
240
z_{phot}=1.41
mag (AB)
Wavelength (μm)
240
ODDS = 0.95
Template
SB2
SB3
Irr
Scd
Sbc
Ell
Redshift
243
z_{phot}=7.89
mag (AB)
Wavelength (μm)
243
ODDS = 0.99
Template
Redshift
508
z_{phot}=7.98
mag (AB)
Wavelength (μm)
508
ODDS = 0.58
Template
Redshift
510
z_{phot}=2.51
mag (AB)
Wavelength (μm)
510
ODDS = 0.93
Template
Redshift

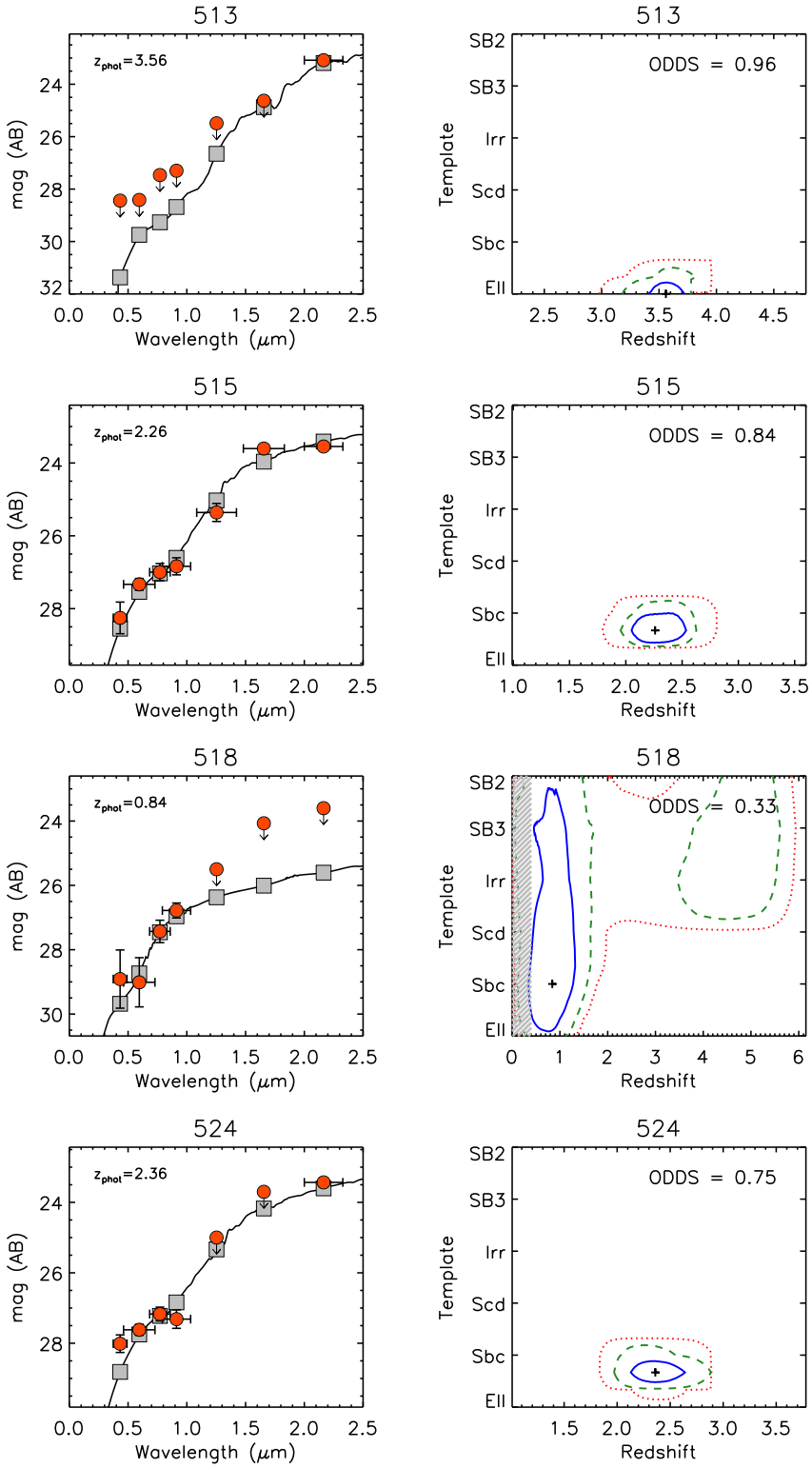
513
z_{phot}=3.56
mag (AB)
Wavelength (μm)
513
ODDS = 0.96
Template
SB2
SB3
Irr
Scd
Sbc
Ell
Redshift
515
z_{phot}=2.26
mag (AB)
Wavelength (μm)
515
ODDS = 0.84
Template
Redshift
518
z_{phot}=0.84
mag (AB)
Wavelength (μm)
518
ODDS = 0.33
Template
Redshift
524
z_{phot}=2.36
mag (AB)
Wavelength (μm)
524
ODDS = 0.75
Template
Redshift

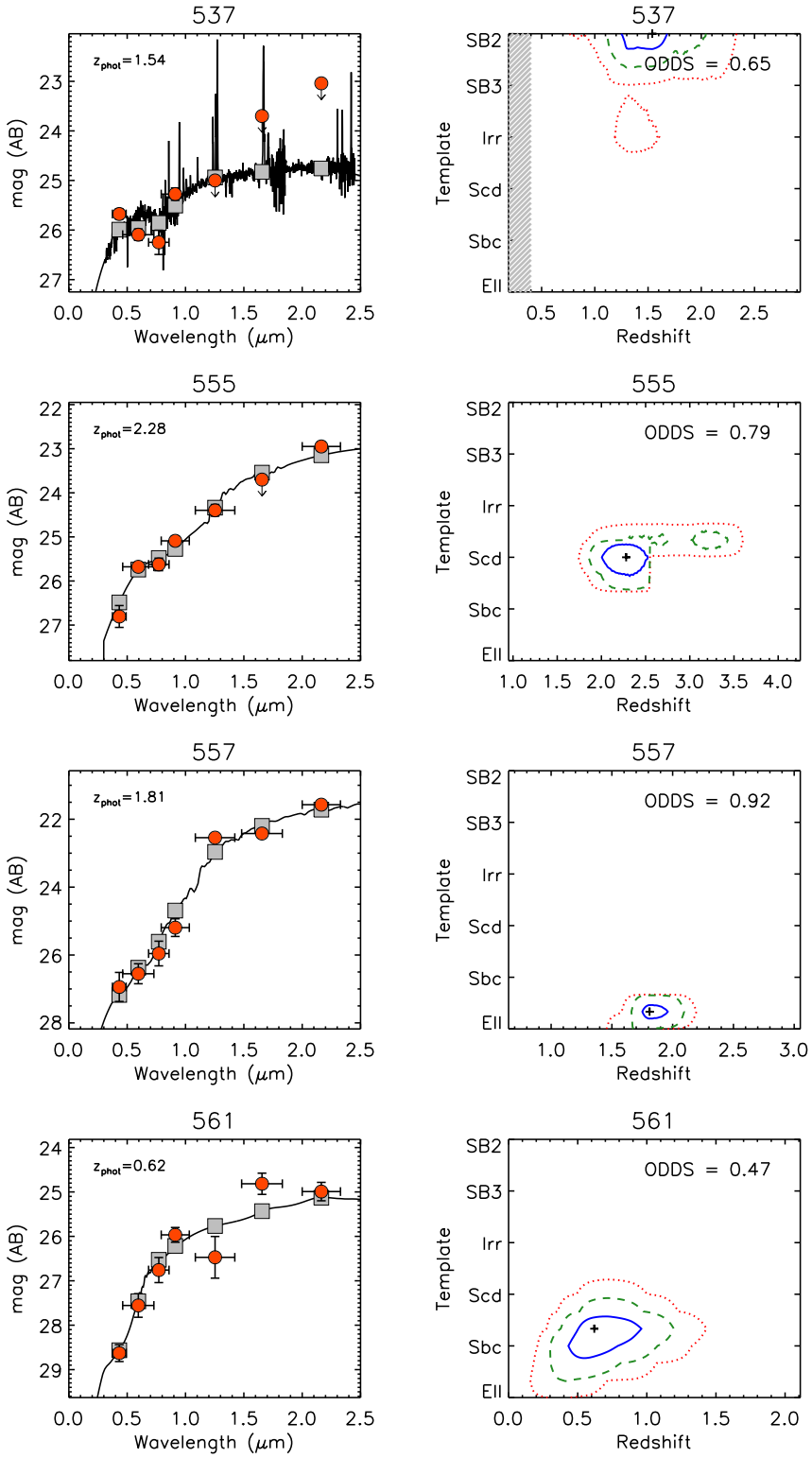
537
z_{phot}=1.54
mag (AB)
Wavelength (μm)
537
ODDS = 0.65
Template
SB2
SB3
Irr
Scd
Sbc
Ell
Redshift
555
z_{phot}=2.28
mag (AB)
Wavelength (μm)
555
ODDS = 0.79
Template
Redshift
557
z_{phot}=1.81
mag (AB)
Wavelength (μm)
557
ODDS = 0.92
Template
Redshift
561
z_{phot}=0.62
mag (AB)
Wavelength (μm)
561
ODDS = 0.47
Template
Redshift

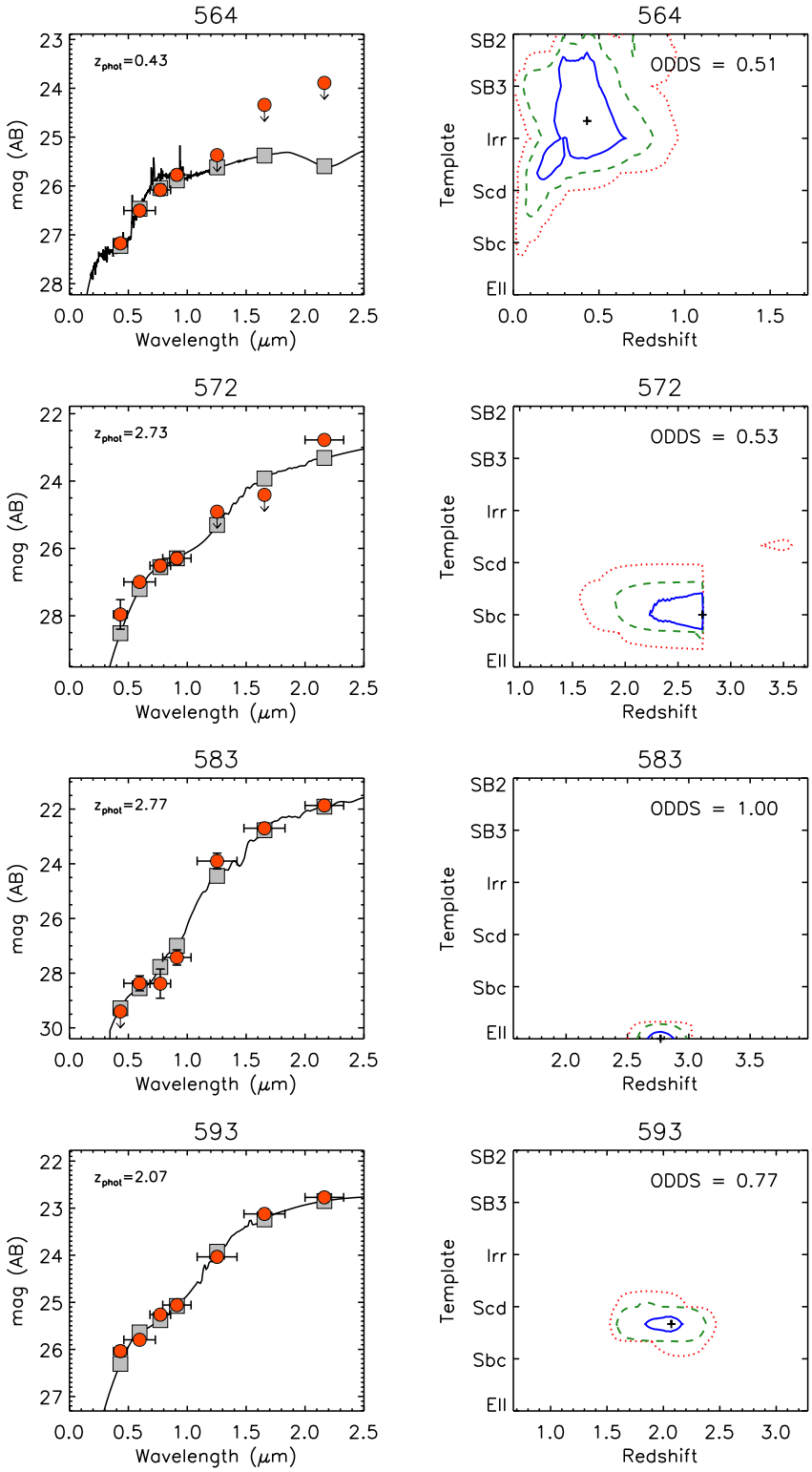
564
z_{phot}=0.43
mag (AB)
Wavelength (μm)
564
ODDS = 0.51
Template
SB2
SB3
Irr
Scd
Sbc
Ell
Redshift
572
z_{phot}=2.73
mag (AB)
Wavelength (μm)
572
ODDS = 0.53
Template
Redshift
583
z_{phot}=2.77
mag (AB)
Wavelength (μm)
583
ODDS = 1.00
Template
Redshift
593
z_{phot}=2.07
mag (AB)
Wavelength (μm)
593
ODDS = 0.77
Template
Redshift

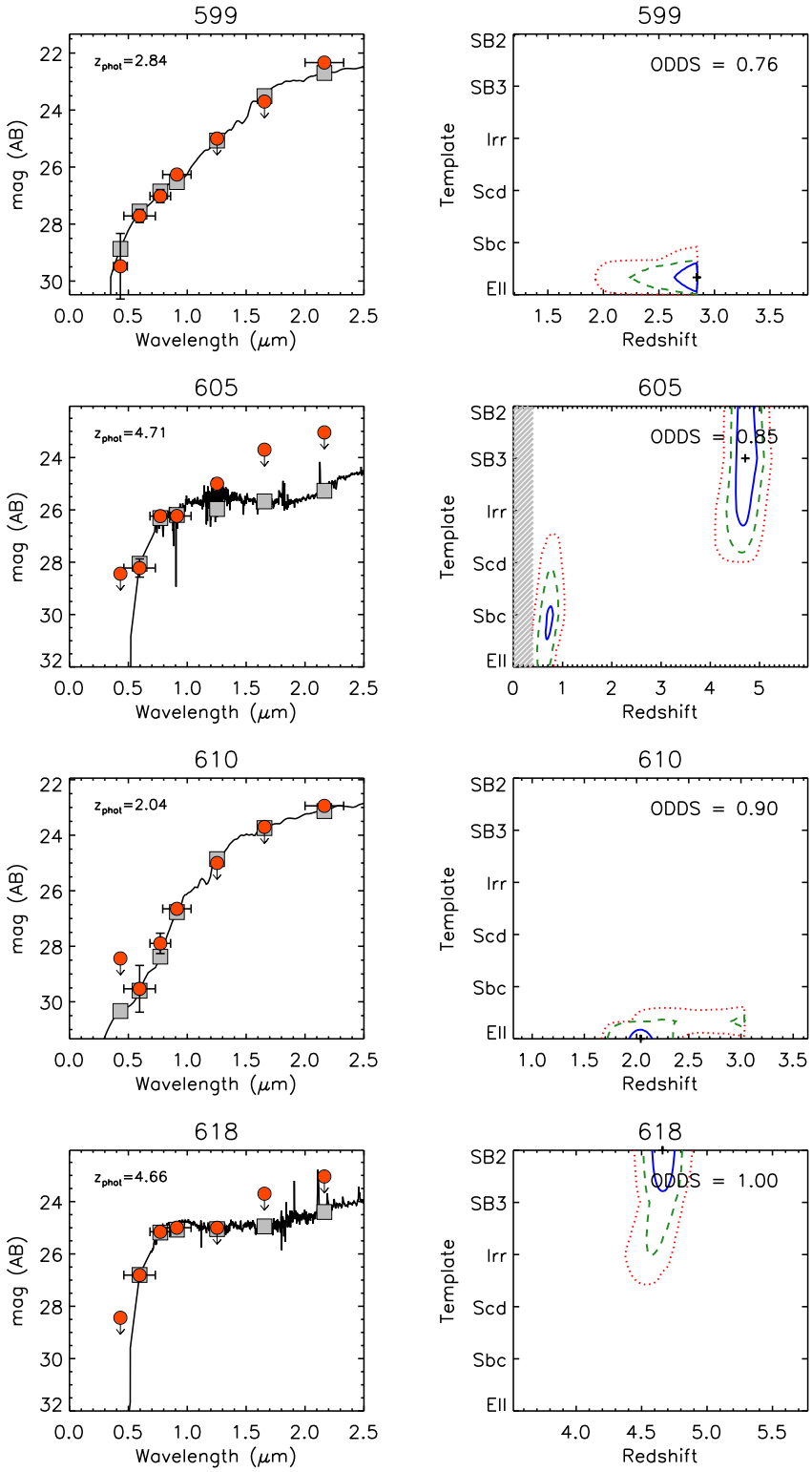
599
z_{phot}=2.84
mag (AB)
Wavelength (μm)
599
ODDS = 0.76
Template
SB2
SB3
Irr
Scd
Sbc
Ell
Redshift
605
z_{phot}=4.71
mag (AB)
Wavelength (μm)
605
ODDS = 0.85
Template
Redshift
610
z_{phot}=2.04
mag (AB)
Wavelength (μm)
610
ODDS = 0.90
Template
Redshift
618
z_{phot}=4.66
mag (AB)
Wavelength (μm)
618
ODDS = 1.00
Template
Redshift

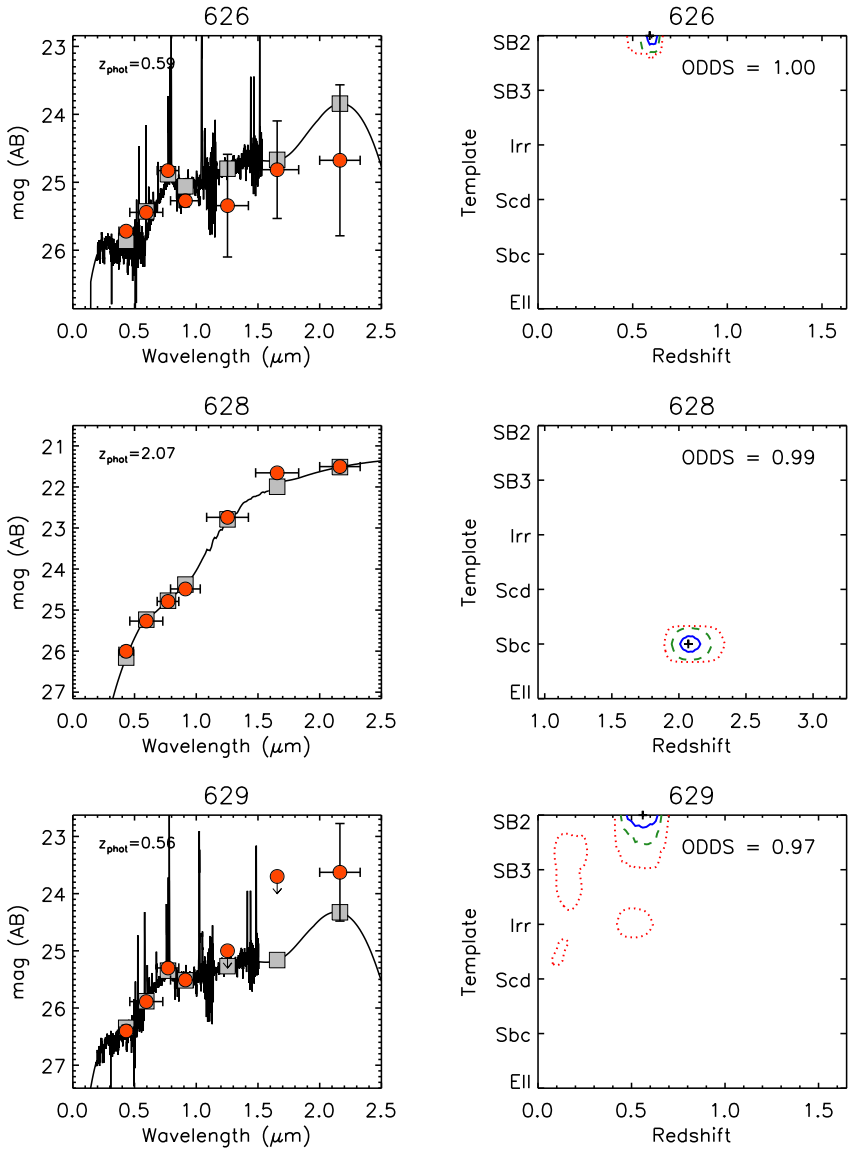
626
z_{phot}=0.59
mag (AB)
Wavelength (μm)
626
ODDS = 1.00
Template
Redshift
628
z_{phot}=2.07
mag (AB)
Wavelength (μm)
628
ODDS = 0.99
Template
Redshift
629
z_{phot}=0.56
mag (AB)
Wavelength (μm)
629
ODDS = 0.97
Template
Redshift
SB2
SB3
Irr
Scd
Sbc
Ell